



Probabilistic forecasting of plausible debris flows from Nevado de Colima (México) using data from the Atenquique debris flow, 1955

Andrea Bevilacqua^{1,2}, Abani K. Patra^{3,2}, Marcus I. Bursik¹, E. Bruce Pitman⁴, José Luis Macías⁵, Ricardo Saucedo⁶, and David Hyman¹

¹*Department of Earth Sciences, SUNY at Buffalo, NY, 14260*

²*Computational Data Science and Engineering program, SUNY at Buffalo, NY, 14260*

³*Department of Mechanical and Aerospace Engineering, SUNY at Buffalo, NY, 14260*

⁴*Department of Materials Design and Innovation, SUNY at Buffalo, NY, 14260*

⁵*Departamento de Vulcanología, Instituto de Geofísica, UNAM, DF, 04510*

⁶*Instituto de Geología, Facultad de Ingeniería, UASLP, SLP, 78240*

Correspondence: Andrea Bevilacqua (bev87@hotmail.it)

Abstract. We detail a new prediction-oriented procedure aimed at volcanic hazard assessment based on geophysical mass flow models constrained with heterogeneous and poorly defined data. Our method relies on an itemized application of the empirical falsification principle over an arbitrarily wide envelope of possible input conditions. We thus provide a first step towards a objective and partially automated experimental design construction. In particular, instead of fully calibrating model inputs on past observations, we create and explore more general requirements of consistency, and then we separately use each piece of empirical data to remove those input values that are not compatible with it, hence defining partial solutions to the inverse problem. This has several advantages compared to a traditionally posed inverse problem: (i) the potentially non-empty inverse images of partial solutions of multiple possible forward models characterize the solutions to the inverse problem; (ii) the partial solutions can provide hazard estimates under weaker constraints, potentially including extreme cases that are important for hazard analysis; (iii) if multiple models are applicable, specific performance scores against each piece of empirical information can be calculated. We apply our procedure to the case study of the Atenquique volcanoclastic debris flow, which occurred on the flanks of Nevado de Colima volcano (México), 1955. We adopt and compare three depth averaged models currently implemented in the TITAN2D solver, available from vhub.org. The associated inverse problem is not well-posed if approached in a traditional way. We show that our procedure can extract valuable information for hazard assessment, allowing the exploration of the impact of synthetic flows similar to those that occurred in the past, but different in plausible ways. The implementation of multiple models is thus a crucial aspect of our approach, as they can allow the covering of other plausible flows. We also observe that model selection is inherently linked to the inversion problem.



1 Introduction

Hazard assessment of geophysical mass flows, such as landslides or pyroclastic flows, usually relies on the reconstruction of past flows that occurred in the region of interest. The available pieces of data $D_i \in \mathcal{D}$, are commonly related to the properties of the deposit left by the flows, and to historical documentation. In general, this information can be affected by relevant sources of uncertainty (e.g., erosion and re-mobilization, superposition of subsequent events, unknown duration and source). Physical models provide us with a deterministic system to relate inputs and outputs of the dynamical system of the mass flow (Gilbert, 1991; Patra et al., 2018a) and are traditionally used to explore “what-if” scenarios and more recently in ways to supplement observed data with physically consistent synthetic data (Bayarri et al., 2015) for probabilistic analysis.

In a probabilistic framework, for each model $M \in \mathcal{M}$ we define (M, P_M) , where P_M is a probability measure over the parameter space of M . While the support of P_M can be restricted to a single value by solving an inverse problem for the optimal reconstruction of a particular flow, the inverse problem is not always well-posed (Tarantola and Valette, 1982; Tarantola, 1987). That is, no input data, or multiple input data, are able to produce outputs consistent with the observed information. Sometimes the strict replication of a past flow may lead to overconstraining the model, especially if we are interested in the general predictive capabilities of a model over a whole range of possible future events. In this study, we generalize a poorly constrained inverse problem, decomposing it into a hierarchy of simpler problems. Our purpose is to provide a new prediction-oriented formulation for use in hazard assessment problems.

1.1 Probabilistic description

Our approach is characterized by three steps:

1. For each model $M_j \in \mathcal{M}$, we initially set up a uniformly probabilized *general input space* that we define as arbitrarily wide, namely $(\Omega_0^j, \mathcal{F}_0^j, P_0^j)$. At this stage, we only require essential properties of feasibility in the models, namely the existence of the numerical output and the realism of the underlying physics.
2. After a preliminary screening, we characterize a *specialized input space* $\Omega^j \subseteq \Omega_0^j$, under additional requirements of plausibility¹ that are related to the macroscopic properties of the outputs. For instance, a robust numerical simulation without spurious effects, meaningful flow dynamics, and/or the capability to inundate a designated region.
3. Through more detailed testing, $\forall i \in I$, we can thus define the subspace $\Omega_i^j \subseteq \Omega^j$ of the inputs that are consistent with a piece of empirical data D_i .

We remark that the specialized input space is the inverse image of the set of plausible outputs D_G through the input-output functions f_j characterizing the models (see following section). We also note that, $\forall j$, all the described subspaces of Ω_0^j , if not negligible, are trivially probabilized by the measures P^j and P_i^j , defined by:

$$P_i^j(A) = P^j(A) / P_0^j(\Omega_i^j),$$

¹our notion of *output plausibility* is not related to the *model plausibility* defined in (Farrell et al., 2015)



for each measurable set $A \in \mathcal{F}_i^j := \left\{ \Omega_i^j \cap B : B \in \mathcal{F}_0^j \right\}$.

The philosophy of our method is based on an itemized application of the empirical falsification principle of K.R. Popper (Popper, 1959), over an arbitrarily wide envelope of possible input conditions. The construction of the subspaces $(\Omega_i^j)_{i \geq 1}$ has several advantages compared to a traditionally posed inverse problem:

- 5 – the intersection space $\Theta^j := \bigcap_i \Omega_i^j$ describes the set of the inputs that solves the inverse problem;
- the partial solutions $(\Omega_i^j)_{i \geq 1}$ provide information concerning flows that partially solve the inverse problem, and they may exist even if $\Theta^j = \emptyset$;
- each probability $P^j(\Omega_i^j)$ represents a performance score of the adopted model against the piece of empirical data D_i , and can therefore be used for model selection purposes.

10 1.2 Functional structures

Our meta-modeling framework is fully described in Figure 1. Let us assume that each model $M_j \in \mathcal{M}$ is represented by an operator:

$$f_{M_j} : \Omega_0^j \longrightarrow \mathbb{R}^d,$$

where $d \in \mathbb{N}$ is a dimensional parameter which is independent on the model chosen, and characterizes a common output space. We also define the global set of feasible inputs:

$$\Omega_G := \bigsqcup_j \Omega_0^j.$$

This puts all the models in a natural meta-modeling framework. Then, we characterize the codomain $D_G \subset \mathbb{R}^d$ of plausible outputs, that is the target of our simulations - it includes all the outputs consistent with the observed data, plus additional outputs which differ in arbitrary, but plausible ways. For the sake of simplicity, we use the same notation for each piece of data D_i and the set of outputs consistent with it. Then $\forall j$, the specialized input space is defined by:

$$\Omega^j = f_{M_j}^{-1}(D_G).$$

In a similar way, $\forall i$, $\Omega_i^j = f_{M_j}^{-1}(D_i)$, and for this reason those sets are called partial solutions to the inverse problem.

We remark that the implementation of multiple models is a crucial aspect in our approach. Typically, the available models are not able to entirely cover D_G , and:

$$D_G \setminus \bigcup_j f_{M_j}(\Omega_0^j) \neq \emptyset.$$

The investigation of D_G and the quality of the solutions will clearly improve as we add more models based on new knowledge of the underlying processes, especially when there is uncertainty as to which model is best in a particular situation. We show that the solution of the partial inverse problems and model selection are strongly linked.

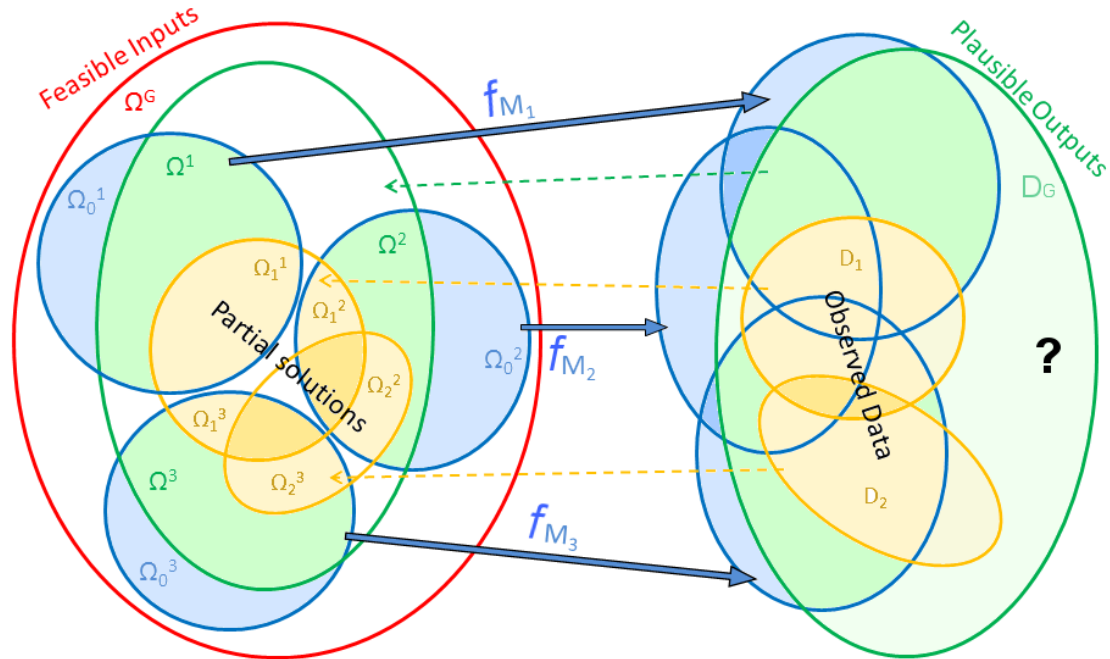


Figure 1. Diagram of input spaces, model functions, and output space (blue), with feasible inputs domain (red), plausible output codomain and specialized inputs (green), and observed data and partial solutions subsets (orange). The question mark emphasizes that the covering of other plausible outputs could be enabled, adding more models if necessary.

1.3 Geophysical case study

We apply our procedure to the case study of the Atenquique volcanoclastic debris flow, which occurred on the flanks of Nevado de Colima volcano (México) in 1955. We adopt and compare the three depth averaged models *Mohr-Coulomb* (MC) (Savage and Hutter, 1989), *Pouliquen-Forterre* (PF) (Pouliquen, 1999; Forterre and Pouliquen, 2002; Pouliquen and Forterre, 2002) and *Voellmy-Salm* (VS) (Voellmy, 1955; Salm et al., 1990), based on the Saint-Venant equations. Input spaces are explored by Monte Carlo simulation based on Latin Hypercube sampling (McKay et al., 1979; Owen, 1992b; Stein, 1987; Ranjan and Spencer, 2014; Ai et al., 2016). The three models are incorporated in our large scale mass flow simulation framework TITAN2D (Patra et al., 2005, 2006; Yu et al., 2009; Aghakhani et al., 2016; Patra et al., 2018b). So far, TITAN2D has been successfully applied to the simulation of different geophysical mass flows with specific characteristics (Sheridan et al., 2005; Rupp et al., 2006; Norini et al., 2009; Charbonnier and Gertisser, 2009; Procter et al., 2010; Sheridan et al., 2010; Sulpizio et al., 2010; Capra et al., 2011). Several studies involving TITAN2D were also directed towards statistical study of geophysical flows, focusing on uncertainty quantification (Dalbey et al., 2008; Dalbey, 2009; Stefanescu et al., 2012a, b), or on the more efficient production of hazard maps (Bayarri et al., 2009; Spiller et al., 2014; Bayarri et al., 2015; Ogburn et al., 2016).

The rest of the study is organized as follows. In section 2, we present our case study - debris flows from Nevado de Colima; in section 3, we introduce the physical models, we define and parameterize their input spaces, and we design our Monte Carlo



simulation; in section 4 we statistically describe the characteristics of the outputs and contributing variables, mapping them globally and detailing them locally. Finally, in section 5, we use multiple pieces of information regarding an historical debris flow to condition the input space, and then we compare the performance of the models over that space. The results show that model selection is inherently linked to the inversion problem, that is, model performance depends on which of the observed data we seek to reproduce. This is a fundamental aspect to consider in the development of multi-model solvers, dynamically selecting the model based on performance against local data.

2 Nevado de Colima volcano and Barranca de Atenquique

The Colima Volcanic Complex is located in the western portion of the Trans-Mexican Volcanic Belt (small box in Fig. 2). It consists of a N–S volcanic chain formed by Cántaro, Nevado de Colima, and Colima volcanoes, within the Colima Graben (Luhr and Carmichael, 1990). It began forming 1.7 Ma ago with the growth of Cántaro Volcano (2800 m.a.s.l.), and continued with the formation of Nevado de Colima volcano 0.53 Ma ago (Allan, 1986; Robin et al., 1987). Activity was intermittent during the Pleistocene and Holocene and continues today at Colima volcano (3860 m.a.s.l.), south of Nevado (Saucedo et al., 2010; Zobin et al., 2015; Macorps et al., 2018).

Nevado de Colima (4320 m.a.s.l.) occupies the central part of the volcanic complex, being the most voluminous of the three volcanoes (300–400 km³). It is characterized by three or four horseshoe-shaped craters (Cortés et al., 2010). The youngest crater is 4 km wide and opens to the east with 100 m deep, vertical walls. This structure contains the summit Picacho dome (4300 m). The eastern flank of Nevado exposes a thick sequence of debris flow, fluvial, pyroclastic flow and debris avalanche deposits known as the Atenquique Formation (Mooser, 1961; Cortés et al., 2005; Saucedo et al., 2008), covered by younger deposits. The crater morphology directs a large part of the drainage from the volcano into the Atenquique ravine, located on the ENE flank of the volcano and ~25 km long. Figure 2 shows the ravine and its surrounding topography.

Plot (2b) includes elevation isolines from the SRTM DEM of 30-m cell size for UTM Zone 13N (NASA (JPL), 2014). The drainage begins at an elevation of 4000 m on the eastern flank of Nevado, is occupied by the perennial Atenquique river, and ends at its junction with the perennial Tuxpan River at 1040 m. Between, 4000 and 2000 m in altitude, the ravine has an average slope of 34°. At an elevation of 1800 m, the Atenquique ravine is cut off by a 250 m cliff in the vicinity of the junction with the Dos Volcanes dry ravine. Beyond this cliff, the slope of the ravine suddenly decreases from 34° to 18°, keeping this gradient to an elevation of 1600 m at 11.5 km from the summit. Between this site and the catchments of the Los Plátanos and Arroyo Seco dry ravines, located at ~21.5 km at an elevation of 1120 m, the ravine gradient varies from 10° to 6°. The town of Atenquique is located at an altitude of 1050 m, and 18.5 km (25 km along the ravine path) from the head of the ravine. There, the ravine channel has a gradient of 5°, which is maintained down to the confluence with the Tuxpan River. Atenquique ravine has an average width of 30 m, although in the vicinity of Atenquique village it is up to 200 m wide.



BARRANCA DE ATENQUIQUE

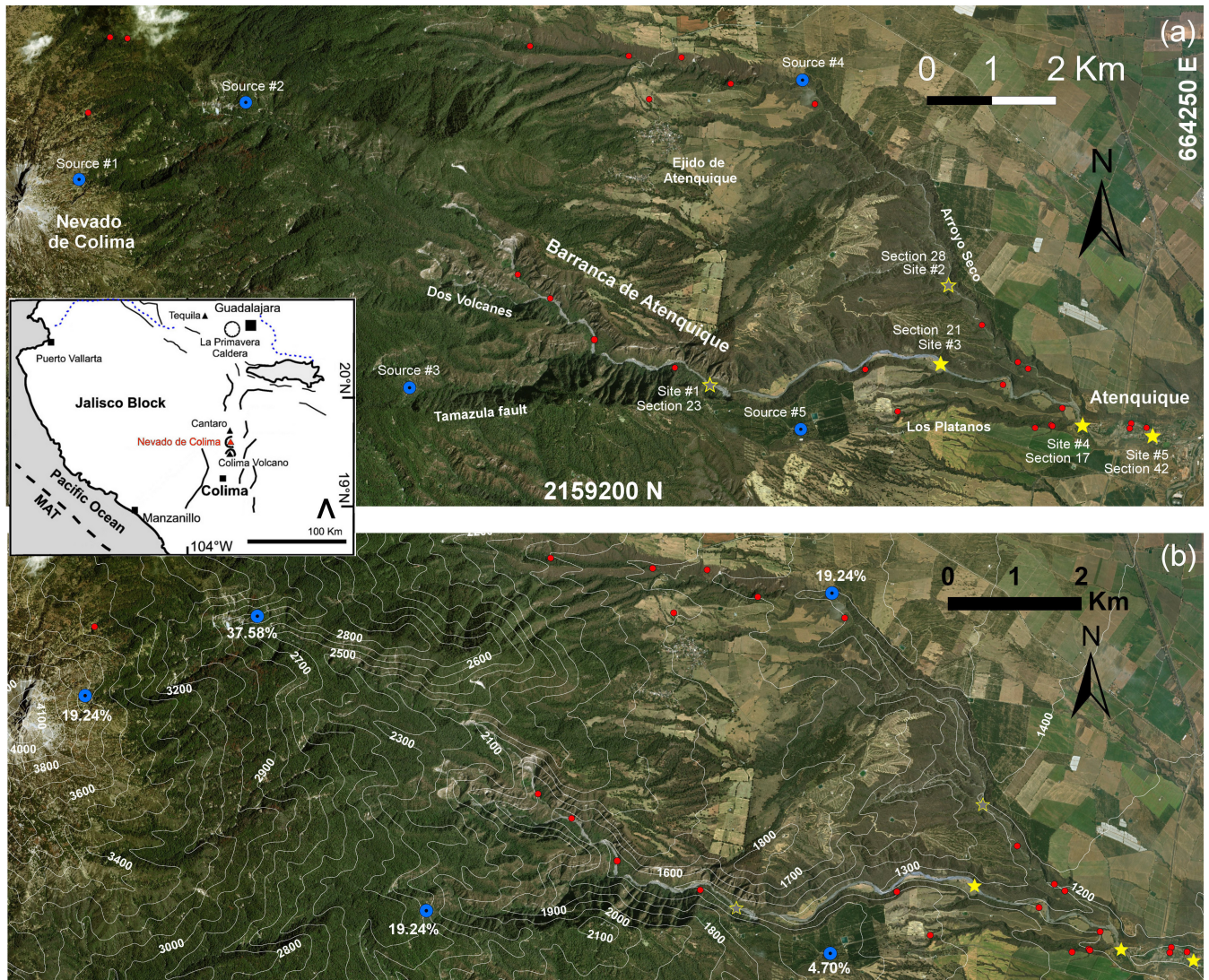


Figure 2. Barranca de Atenquique (México) overview. (a) Stratigraphic sections of (Saucedo et al., 2008) are marked with red dots, including 5 preferred locations (stars) and major ravines. Shaded sites are detailed in Supporting Information. Initial source piles are marked by blue dots. Coordinates and projection are UTM zone 13N WGS84. (b) Digital elevation map including isolines (NASA (JPL), 2014). Volume partition percentages among sources are reported. Regional map is included in a small box.

2.1 The Atenquique volcanoclastic debris flow, 1955

On 16 October, 1955, at 10:45 am, the inhabitants of Atenquique were surprised by the sudden arrival of an 8–9-m high wave carrying mud, boulders and tree trunks that devastated the buildings in the town and four bridges, including the railroad bridge. More than 23 people died, and the flood leveled everything but the tower of the church and the upper part of the market place



that luckily served as shelter for survivors (Ponce-Segura, 1983; Saucedo et al., 2008). During the peak flow, eyewitnesses observed that complete walls of buildings were displaced several meters by the flood prior to their collapse. The deposits are exposed along the Atenquique, Arroyo Seco, Los Plátanos and Dos Volcanes ravines, and their distribution, stratigraphy, granulometry, and volume have been described in Saucedo et al. (2008). Sixty stratigraphic sections were studied along the
5 Atenquique ravine and its main tributaries (Fig. 2). Deposits cover a minimal area of 1.2 km^2 , and with an average thickness of 4 m, a minimum volume of $3.2 \times 10^6 \text{ m}^3$ was estimated for the flow.

The main flood probably formed in the Atenquique ravine, but was enhanced by the confluence of flows from its tributaries: Dos Volcanes at 11.2 km, Arroyo Seco and Los Plátanos, at 22.5 km. During the first 10 km (as recorded by the proximal exposures) the flow moved down steep slopes, eroding and incorporating coarse alluvium and sand. Downstream, in the medial
10 exposures, the flow encountered gentler slopes, reducing its velocity and promoting deposition of part of the sediment load. Just upstream of the village, below the junction with the Arroyo Seco and Los Plátanos ravines, eyewitnesses reported peak flood levels, possibly enhanced by the engulfing of a small water reservoir. At the junction, the flow captured the fine-material load of flow from the Arroyo Seco and Plátanos ravines, causing significant dilution and a sudden increase in the flow turbulence. Downstream from the town, the flow lost its capacity to transport large boulders, probably due to widening of the flow and the
15 consequent fall in velocity, which was further reduced by the hydraulic roughness effects of the flow impacting buildings. The diluted flow probably had a velocity in the range of 4 to 6 m/s, obtained by comparison with analogous flows (Pierson, 1985; Saucedo et al., 2008). The flood finally continued downstream to join with the perennial Tuxpan River, where it emplaced up to 6 m of deposits.

2.2 Multiple sources and their locations

The 1955 debris flow, according to eyewitness accounts and deposit analyses, emanated from multiple sources throughout the watershed. The existence of multiple source areas presents a unique challenge when attempting to model the flow. Eyewitnesses confirm that after the event, many small landslides scars were present along the main ravine and its tributaries. It is hypothesized that these landslides, triggered by rain infiltration, supplied the bulk of the material (Saucedo, 2003; Saucedo et al., 2008). To account for this, and based on the work in Rupp (2004) we initiate the flow from five major source locations, reported in Fig. 2. We remark that our numerical simulation toolkit allows for multiple starting points in the same run. Each source consists of a paraboloid pile of material with unitary aspect ratio. Two source locations (#1 and #2) are placed in the main ravine, one (#3) in a lateral valley associated with the regional Tamazula fault, one source (#4) in Arroyo Seco and one (#5) in Arroyo Plátanos. These locations are selected based upon local topography. The first three are located on steep upland slopes, while the other two are located along the main drainage due to the lack of steep terrain nearby (Rupp, 2004). The partition of volume $V = \sum_{k=1}^5 V_k$ among the five sources is scaled based upon the size of the drainage basin they are located within. In particular, $\forall k$ we define $w_k = V_k/V$ as:

$$w_1 = w_3 = w_4 = 19.24\%, \quad w_2 = 37.58\%, \quad w_5 = 4.70\%.$$

20 This is equivalent to choosing pile radii of 80 m, 100 m and 50 m respectively.



We remark that source number, location, and volume partition will be preserved in the following analysis. However, we tested whether small variations affect the character of the simulated flow only proximally. Large variations, for example additional testing focused on increasing the weight w_4 of the source in Arroyo Seco are not excluded, but would require additional field work to be constrained, and are beyond the purpose of this study. More details about volume V are provided in Section 3.1.

5 3 Prediction-oriented probabilistic modeling

Our numerical modeling of the Atenquique flow proceeds by first assuming that the laws of mass and momentum conservation hold for properly defined system boundaries. The flow had very small depth compared to its length, and hence we assume that it is reasonable to integrate through the depth to obtain simpler and more computationally tractable equations (Savage and Hutter, 1989). The depth-averaged Saint-Venant type equations that result are:

$$\begin{aligned}
 10 \quad & \frac{\partial h}{\partial t} + \frac{\partial}{\partial x}(h\bar{u}) + \frac{\partial}{\partial y}(h\bar{v}) = 0 \\
 & \frac{\partial}{\partial t}(h\bar{u}) + \frac{\partial}{\partial x}\left(h\bar{u}^2 + \frac{1}{2}kg_z h^2\right) + \frac{\partial}{\partial y}(h\bar{u}\bar{v}) = S_x \\
 & \frac{\partial}{\partial t}(h\bar{v}) + \frac{\partial}{\partial x}(h\bar{u}\bar{v}) + \frac{\partial}{\partial y}\left(h\bar{v}^2 + \frac{1}{2}kg_z h^2\right) = S_y
 \end{aligned} \tag{1}$$

Here the Cartesian coordinate system is aligned such that z is normal to the surface; h is the flow depth in the z direction; $h\bar{u}$ and $h\bar{v}$ are respectively the components of momentum in the x and y directions; and k is the coefficient which relates the lateral stress components, $\bar{\sigma}_{xx}$ and $\bar{\sigma}_{yy}$, to the normal stress component, $\bar{\sigma}_{zz}$. Note that $\frac{1}{2}kg_z h^2$ is the contribution of hydrostatic pressure to the momentum fluxes. S_x and S_y are the sum local stresses: their definition depends on the constitutive model of the flowing material (Kelfoun, 2011). These include the gravitational driving forces, the basal friction force resisting to the motion of the material, and additional forces specific of rheology assumptions.

In this study we adopt the *Mohr-Coulomb* (MC), *Pouliquen-Forterre* (PF) and *Voellmy-Salm* (VS) models, detailed in Appendix A. These three models for large scale mass flows are incorporated in our large scale mass flow simulation framework TITAN2D (Patra et al., 2005). The 4th release of TITAN2D ² offers multiple rheology options in the same code base. The availability of three distinct models for similar phenomena in the same tool provides us with the ability to directly compare outputs and internal variables in all the three models and control for usually difficult to quantify effects like numerical solution procedures, input ranges and computer hardware (Patra et al., 2018b).

25 3.1 Preliminary definition of the input space

The definition of the input space hierarchy $\mathbb{R}_+^{d_j} \supseteq \Omega_0^j \supseteq \Omega^j \supseteq \Omega_i^j, \forall i, j$, is a fundamental part of our approach. The dimensionality d_j is a characteristic of the model. The input spaces of MC and VS have three dimensions, and are therefore parameterized:

$$\Omega_0^{\text{MC}} = \{(\phi_{bed}, \phi_{int}, V) \in \mathbb{R}_+^3\},$$

²available from vhub.org



$$\Omega_0^{\text{VS}} = \{[\arctan(\mu), \log_{10}(\xi), V] \in \mathbb{R}_+^3\}.$$

On the other hand, the input space of model PF originally has six dimensions - $(\phi_1, \phi_2, \phi_3, \beta, L, V)$. Following Pouliquen and Forterre (2002), we constrain $\phi_3 = \phi_1 + 1^\circ$. Moreover, preliminary testing in our case study showed a very similar impact from the variation of β and L . So, we were able to further reduce $d_{\text{PF}} = 4$, by assuming the empirical relationship:

$$\beta = f(\phi_2) := \frac{\phi_2 - 7^\circ}{20} + 0.1, \quad (2)$$

which is consistent with the β values presented in literature (Pouliquen and Forterre, 2002; Forterre and Pouliquen, 2003). In the following we also show the effect of fixing the value of β . We thus effectively parameterize:

$$\Omega_0^{\text{PF}} = \{(\phi_1, \phi_2, L, V) \in \mathbb{R}_+^4\}.$$

5 3.1.1 General input space

The input space boundaries $(a_{k,M_j}, b_{k,M_j})_{1 \leq k \leq d_j}$ of Ω_0^j are constrained by the general assumptions:

– **Total Volume:** $V \in [3.5, 5] \times 10^6 \text{ m}^3$, i.e. $4.25 \pm 0.75 \times 10^6 \text{ m}^3$.

– **Input space constraints:**

MC - $\phi_{bed} \geq 5^\circ$, $\phi_{int} \in [\phi_{bed}, 45^\circ]$.

10 **PF** - $\phi_1 \geq 1^\circ$, $\phi_2 \in [\phi_1 + 6^\circ, \phi_1 + 18^\circ]$, $L \in [0.1, 0.5] \text{ m}$.

VS - $\arctan(\mu) \geq 1^\circ$, $\log_{10}(\xi) \leq 4$.

In particular, a minimum volume of $3.2 \times 10^6 \text{ m}^3$ for the deposit left by the flow was obtained by Saucedo et al. (2008). We assume that it is reasonable to increase this volume by about 10% to 50% to represent the potential real volume in the simulated flow, given the lack of recovery of any deposit for the portion of the flow reaching the Tuxpan river. We exclude basal friction angles below 5° in MC, and 1° in PF and VS because of numerical instability and unphysical behavior. In MC, we constrain $\phi_{bed} < \phi_{int}$, and we exclude internal friction angles over 45° because these are not considered realistic. In VS we do not allow ξ over 10^4 because it produces unphysical results. In PF we constrain $\phi_1 + 6^\circ < \phi_2 < \phi_1 + 18^\circ$, extending the range of values presented in literature (Pouliquen and Forterre, 2002; Forterre and Pouliquen, 2003). The parameter L is related to the particle size Forterre and Pouliquen (2003), hence we define it consistent with the observed average clasts sampled in the field (Saucedo et al., 2008).

3.1.2 Specialized input space

The construction of Ω_0^j relies on extensive testing of the models over the general input space defined above. We base our analysis on two qualitative properties that any realistic flow must have: (i) the flow must reach the town of Atenquique in a reasonable time, (ii) the flow does not over-top the ravine walls. We quantitatively re-formulate these properties as:



- (i) the flow reaches a minimum elevation $\zeta < 1200$ m a.s.l. before $t = 1200$ s,
- (ii) the maximum over-spill at the confluence of flows from different sources is < 0.1 m thick.

In (i), we selected 1200 m elevation because it is located about 1 km upstream from the village (Saucedo et al., 2008), and $t = 1200$ s, because we observed that flows that require more time are not able to realistically inundate the village. In (ii) we focused on flow confluences because they are where the major over-spilling issues take place in our tests. Small changes in this definition not significantly affect the following analysis.

SPECIALIZED INPUT SPACES

Mohr-Coulomb					
TABLE A		φ_{int} (deg)			
		30	35	40	45
φ_{bed} (deg)	5.5	1170	1150	1120	1100
	6	1230	1200	1180	1130
	6.5	1260	1230	1200	1160
	7		1280	1250	1220

(a)

Voellmy-Salm					
TABLE C		$\log_{10}(\xi)$			
		2.5	3.0	3.5	4.0
$atan(\mu)$ (deg)	1	1220	1020	980	970
	1.5	1260	1060	1010	990
	2	1330	1200	1060	1010
	2.5	1390	1280	1170	1050
	3		1360	1280	1200
	3.5			1370	1280

(b)

Pouliquenne-Forterre (1)						
TABLE B1		L (m)				
		0.1	0.2	0.3	0.4	0.5
φ_1 (deg)	1		1050	1080	1110	1130
	1.5		1090	1120	1150	1170
	2		1140	1170	1200	1220
	2.5		1210	1230	1250	1260

(c)

Pouliquenne-Forterre (2)						
TABLE B2		L (m)				
		0.1	0.2	0.3	0.4	0.5
φ_1 (deg)	1	990	1020	1070	1110	1150
	1.5	1020	1070	1120	1170	1200
	2	1070	1130	1190	1220	1250
	2.5	1150	1220	1260	1280	
	3	1230	1290			

Pouliquenne-Forterre (3)						
TABLE B3		L (m)				
		0.1	0.2	0.3	0.4	0.5
φ_1 (deg)	1	990	1020	1090	1130	1170
	1.5	1020	1090	1150	1200	1230
	2	1070	1160	1220	1260	1290
	2.5	1170	1250	1280		
	3	1250	1330			

Pouliquenne-Forterre (4)						
TABLE B4		L (m)				
		0.1	0.2	0.3	0.4	0.5
φ_1 (deg)	1	990	1050	1110	1170	1220
	1.5	1020	1100	1170	1230	1280
	2	1090	1190	1250	1300	
	2.5	1190	1270	1340		
	3	1260	1360			

Table 1: Input space exploration and testing of (a) MC, (b) VS, (c) PF models, $V = 4.18 \times 10^6 m^3$. The 3D input space of PF is described by four 2D subspaces. Values reported are the minimum elevation ζ reached at $t = 1200$ s. A gray background marks those inputs that generate unphysical flow run-up and over-spill the ravine walls, light gray if > 0.1 m, dark gray if > 1 m. Red lines mark the subdomain^j of flows with $\zeta \leq 1200$ m and without significant over-spill issues.

Table 1 reports the minimum elevation ζ inundated at 1200 s, and a summary of over-spill issues. These values are generated with reference to a flow volume of $V = 4.18 \times 10^6 m^3$, roughly equivalent to the mean value of our range, and so the input spaces have two dimensions in MC and VS, and three in PF. Following the empirical falsification principle, we snip the input range by deleting those regions that do not satisfy our requirements. The subspaces obtained by this procedure do not have rectangular shape, but look like parallelograms - this is because the effects of the input variables on the output are not independent. Maximum flow height maps of all these tests are included in Supporting Information S11-S13.

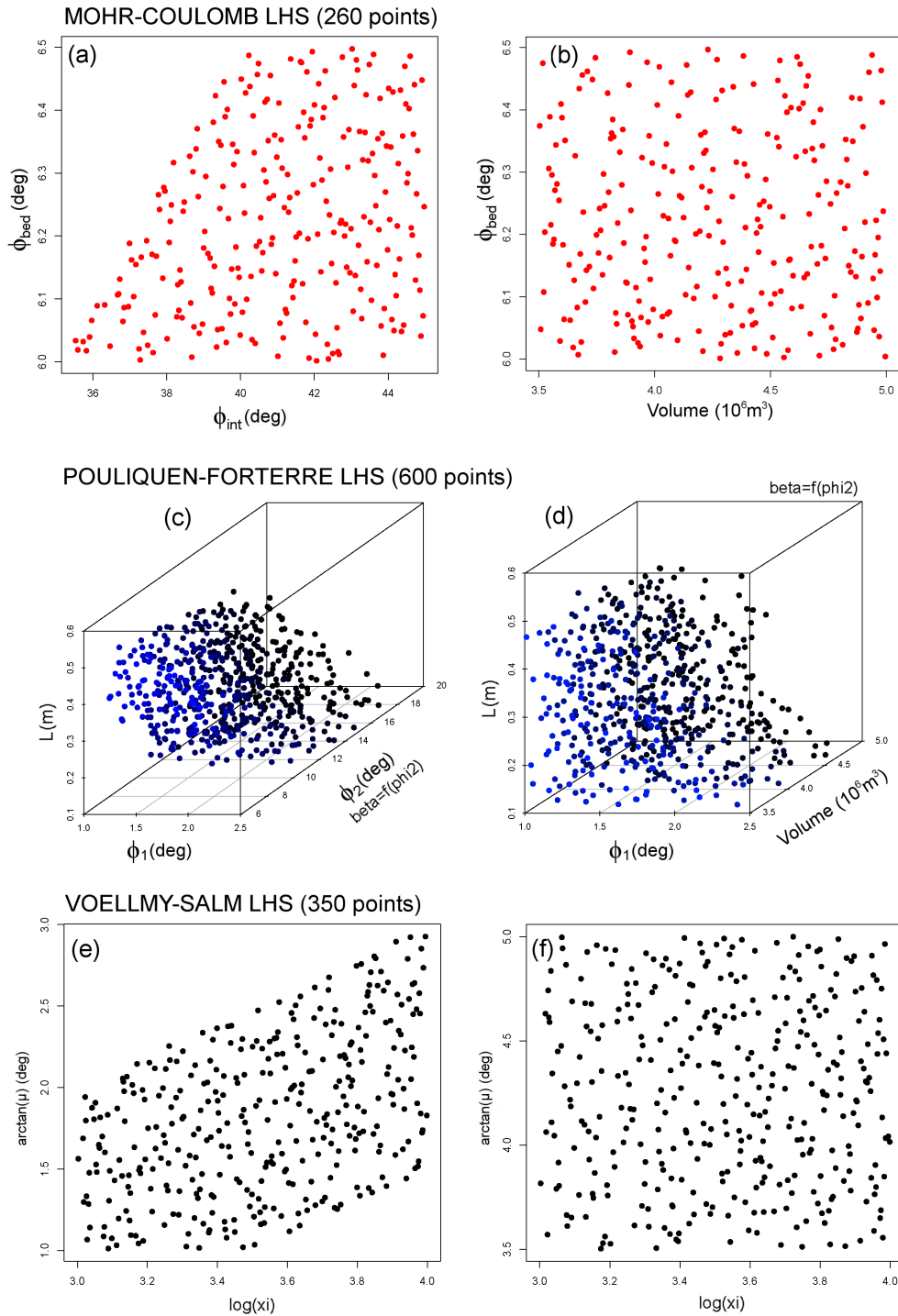


Figure 3. Overview of the specialized experimental design in (a-b) MC, (c-d) PF, (e-f) VS models. (a-c-e) are projected along the V coordinate, and (b-d-f) along ϕ_{int} , ϕ_2 and ξ coordinates, respectively. In (c-d), the color expresses the distance along the third dimension.



- In MC we observe over-spill issues if $\phi_{bed} < 6^\circ$, and a runout that is too short if $\phi_{bed} > 6.5^\circ$. We also note an increase in the runout distance as ϕ_{int} increases. In particular, $\phi_{int} \geq 35^\circ$ is required to inundate the village.
 - In VS the over-spill is observed in the region $\{\arctan(\mu) < 1.5^\circ\} \times \{\log_{10}(\xi) > 3.5\}$.
 In contrast, the region $\{\arctan(\mu) > 3^\circ\} \times \{\log_{10}(\xi) < 3\}$ produces runouts that are too short.
- 5
- Model PF must be treated with greater care because of its higher dimensionality. We divide its behavior along four different hyperplanes, corresponding to different values of ϕ_2 and $\beta = f(\phi_2)$. Over-spill was observed only in the hyperslice with $\phi_2 = 7^\circ$, and $L < 0.4$ m. In general, $\phi_1 < 3^\circ$ is required to have a long-enough runout.

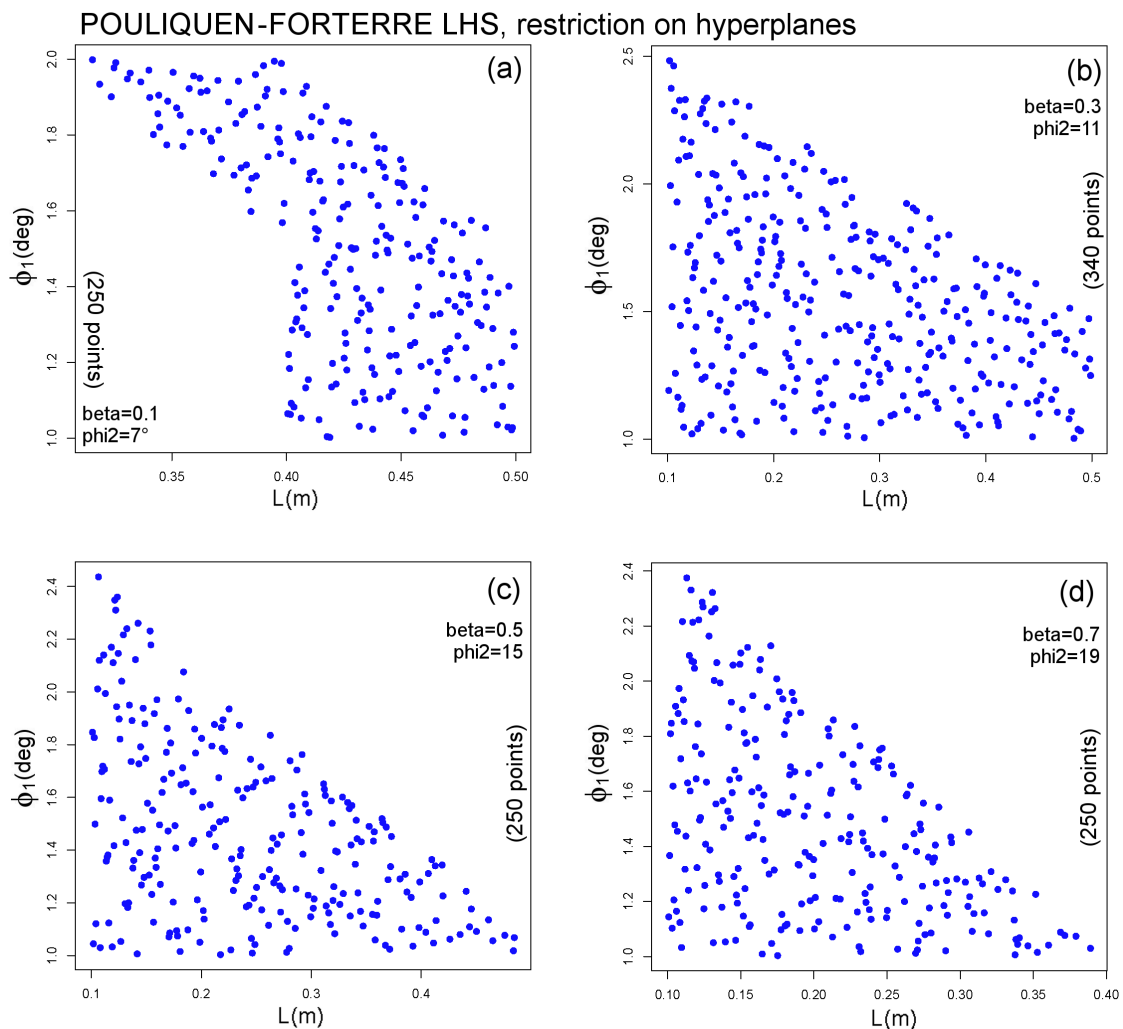


Figure 4. Overview of modified specialized experimental designs in PF, supported over the four different hyperplanes described in Table 1. All plots are projected along the V coordinate.



3.2 Probability measures and specialized experimental design

Initially, $\forall j$ we uniformly distribute the measure P_0^j supported in the general input space $(\Omega_0^j, \mathcal{F}_0^j)$:

$$P_0^j(p_1^j, \dots, p_{d_j}^j) \sim \bigotimes_{k=1}^{d_j} \text{Unif}(a_{k, M_j}, b_{k, M_j}), \quad (3)$$

where $(p_1^j, \dots, p_{d_j}^j)$ is the parametrization of model $M_j \in \mathcal{M}$ described above, and $\forall k, (a_{k, M_j}, b_{k, M_j})$ is the input range. Latin

5 Hypercube Sampling is performed over $[0, 1]^{d_j}$.

We enhance the sampling procedure by relying on orthogonal arrays (Owen, 1992a; Tang, 1993; Patra et al., 2018b). Those dimensionless samples are thus linearly mapped over the required intervals, providing the general experimental design. Then, according to the definition of the specialized input space, we remove the design points which lie outside of the boundary. The new design is distributed according to the subspace probability measure P^j , naturally defined over the σ -field $\mathcal{F}^j :=$
 10 $\{B \cap \Omega^j : B \in \mathcal{F}_0^j\}$.

Figure 3 displays the plot of this specialized experimental design. In PF, the design is embedded in \mathbb{R}^4 , and in Figure 4 we show the plot of ancillary experimental designs supported over the four hyperplanes described in Table 1, corresponding to different values of ϕ_2 and $\beta = f(\phi_2)$. In the following, our time domain is $T = [0, 2400 \text{ s}]$, which provides sufficient time for simulated flows to realistically inundate the village, considering the inputs in Ω^j . We call $t_f = 2400 \text{ s}$, the ending time of the
 15 simulation.

Figure 5 summarizes all the steps of our approach, following the notation defined in the Introduction. We remark that the comparison of observed data to the statistical summary of the outputs can provide some information on possibly untested plausible flows, and on the hypothetical necessity of implementing additional models.

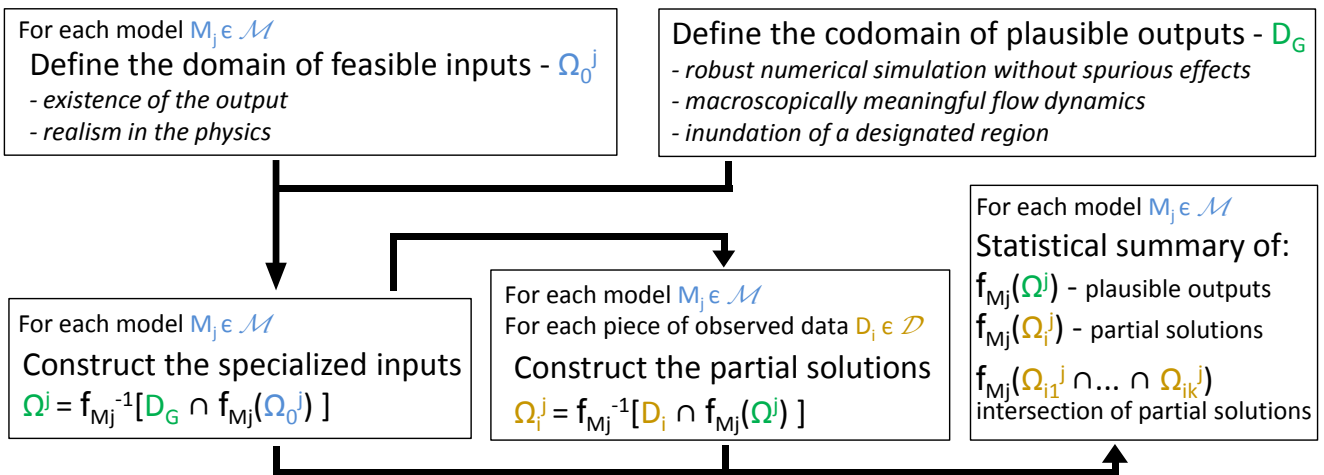


Figure 5. Diagram of the steps of our meta-modeling approach. Our statistical summary includes the local analysis if contributing variables.



4 Observable outputs and contributing variables

We devise multiple statistical measures for analyzing the data according to the specialized LHS design described in the previous section. In general, for each $M_j \in \mathcal{M}$, we sample the model inputs in a Monte Carlo simulation, and the output of each sample run is calculated as a function $f_j(\omega, \mathbf{x}, t)$, where ω is the input, t is the time and \mathbf{x} is a spatial element of the computational grid. The family of these functions naturally defines a random variable which expresses the model outputs with respect to the probability distribution P^j over the input space $(\Omega^j, \mathcal{F}^j)$. This analysis generates a tremendous volume of data that we analyze using statistical methods. The results are summarized by a family of spatial maps and temporal graphs, displaying the expectation of the model outputs and also their 5th and 95th percentiles, with respect to P^j .

In particular, we select five sites and we gather detailed results from our simulations in those special locations. These are called Sites #1-#5 (stars in Figure 1). They all belong to the set of the sixty sections studied in Saucedo et al. (2008), and the corresponding section numbers are also reported. In detail they are:

- **Site #1**, section 23, UTM 656690.1N, 2160985.4E. Along the main ravine ~6 km upstream from the Atenquique village.
- **Site #2**, section 28, UTM 660380.8N, 2162530.8E. In Arroyo Seco tributary ~2.5 km upstream from the confluence.

These first two are not described in detail, but the related results are included in Supporting Information SI4-SI5. Conversely, we focus our analysis on the other three points, all placed along the main ravine in proximity to Atenquique village.

- **Site #3**, section 21, UTM 660258.1N, 2161315.2E. It is ~2 km upstream from the village;
- **Site #4**, section 17, UTM 662453.1N, 2160360.1E. Immediately upstream from the village, close to the confluence with Arroyo Seco and Arroyo Plátanos tributaries;
- **Site #5**, section 42, UTM 663539.0N, 2160200.0E. In the village, ~1 km downstream from the previous site.

We note that close to Site #4 there are the supports of the new bridge of the freeway to the city of Colima.

4.1 Percentile maps of maximum flow depth and kinetic energy

First of all, we report the spatial maps of maximum flow depth, h , and kinetic energy, κ :

$$H := \max_{t \in T} h(x, y), \quad K := \max_{t \in T} \kappa(x, y). \quad (4)$$

In our depth-averaged approach the *kinetic energy*³ is defined as:

$$\kappa := \frac{1}{2} \frac{(h\bar{u})^2 + (h\bar{v})^2}{h}, \quad (5)$$

where $h\bar{u}$ and $h\bar{v}$ are, respectively, the components of momentum in the x and y directions.

³while the use of dynamic pressure is more common in these applications, we have used kinetic energy as a more stable indicator of potential to damage infrastructure and a quantity whose computation as a conserved scalar across all models is more stable.



This is equivalent to $\frac{1}{2}h||(\bar{u}, \bar{v})||^2$, that is half the flow height times the speed square. Thus κ is formally the kinetic energy density per unit of surface area, for a mass with unit density.

MAXIMUM FLOW HEIGHT PERCENTILE MAPS

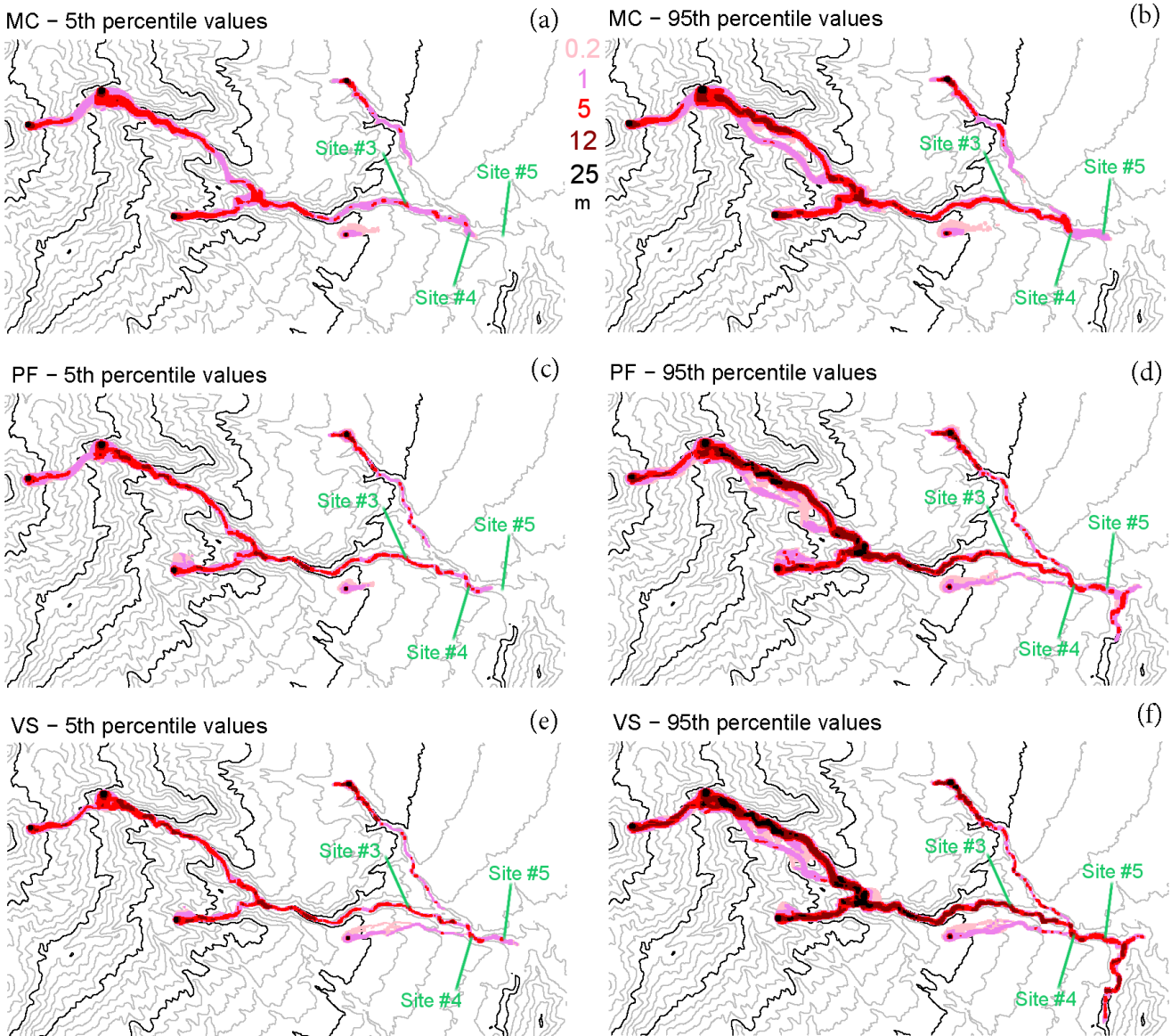


Figure 6. Maximum flow height H as a function of time in (a-b) MC, (c-d) PF, (e-f) VS model. (a-c-e) are the 5th and (b-d-f) are the 95th percentile values with respect to P^j . Colors are related to the flow height. Elevation contours are included at intervals of 100 m (gray) and 500 m (black) (NASA (JPL), 2014). Sites #3,#4,#5 are displayed.



MAXIMUM KINETIC ENERGY PERCENTILE MAPS

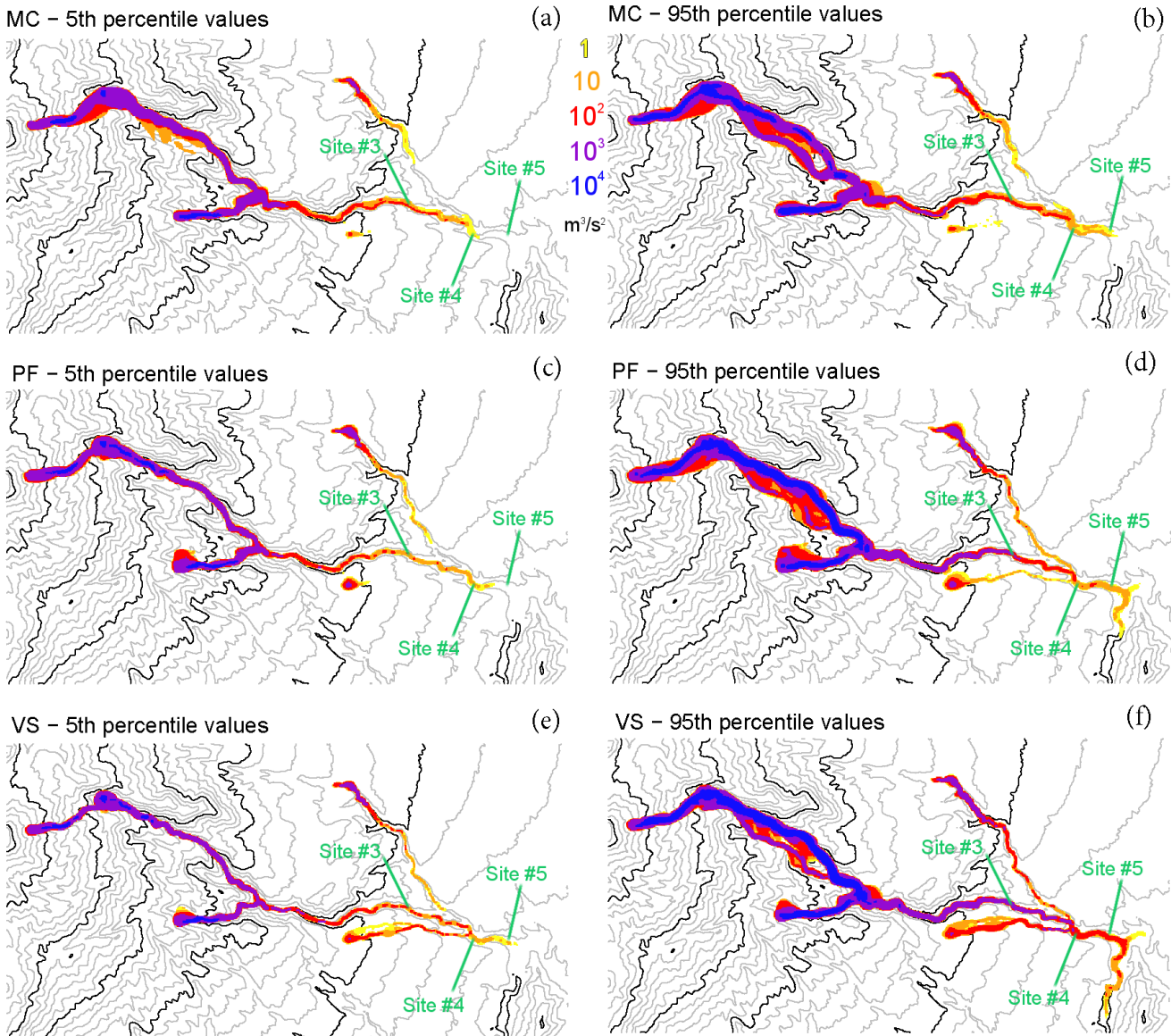


Figure 7. Maximum kinetic energy K as a function of time in (a-b) MC, (c-d) PF, (e-f) VS model. (a-c-e) are the 5th and (b-d-f) are the 95th percentile values with respect to P^j . Colors are related to the energy in logarithmic scale. Elevation contours are included at intervals of 100 m (gray) and 500 m (black) (NASA (JPL), 2014). Sites #3,#4,#5 are displayed.

The kinetic energy, K , in a traditional sense may be calculated over an arbitrary region R as:

$$\text{Kin}(R) = \rho \int_R \kappa(x, y) dx dy = \rho \int_R \frac{1}{2} h(x, y) [\bar{u}(x, y)^2 + \bar{v}(x, y)^2] dx dy,$$



where ρ is the density of the flow, typically in $[1000, 2000] \text{ kg/m}^3$, depending on the flow water content.

Figure 6 reports the maximum flow depth, H , and Figure 7 the maximum kinetic energy, K . MC shows the lowest values of both flow depth and energy, while VS the highest, especially in the distal part of the domain. In MC, the flow in the tributaries is not capable of reaching the village, while in the 95th percentile maps of PF and VS, it is. In VS, the flow in Arroyo Plátanos joins the main ravine even in the 5th percentile map. In general, local maxima of flow depth are located in the ravine, while the kinetic energy shows a more regular decrease. The energy values at the head of the flow are in $[1, 10] \text{ m}^3/\text{s}^2$, meaning a relatively slow flow compared to the dynamics observed upstream. Significant over-spill issues are absent, but in the 95th percentile maps all the models report some flow in the Dos Volcanes ravine, of about $[1, 5] \text{ m}$ maximum height, and slightly less in PF.

10 4.2 Local properties of the flow

We further analyze the flow properties at the three sites selected above, and located in the distal part of the flow (Sites #3,#4, #5), with very different results. All the quantities reported are estimated on the element of the grid which contains the coordinates of the site. We remark that the grid is adaptive, and hence the values can be affected by the size and position of the element. However, the integration over the input space significantly reduces this effect (Patra et al., 2018b).

15 Along with the locally analyzed flow height and speed, we calculate the local *contributing variables* in the modeling equations, that is, the *dominance factors* and the *expected contributions* related to the force terms in the conservation laws that characterize the models. In particular, $\forall n = 1, \dots, N$ the dominance factor, p_n , is the probability that the related force term, F_n , is largest. The no-flow probability, p_0 , is also included, and $\sum_{n=0}^N p_n = 1$. In contrast, $\forall n$ the expected contribution $E^{P_j} [C_n]$ is the mean of the force term, F_n , divided by the greatest (dominant) term. It belongs to $[0, 1]$ and represents the degree of
20 relevance of the n^{th} term with respect to the dominant one. Contributing variables and their statistics are introduced in Patra et al. (2018b) and detailed in Appendix B.

The higher dimensionality of Ω^{PF} requires additional testing. In particular, flow height and speed are estimated on the hyperplane $\beta = 0.5$, $\phi_2 = 15^\circ$, and the probability distributions are not remarkably different. Additional plots concerning sites #1 and #2 are included in SI4-SI5.

25 Figure 8 shows the local properties at site #3, located $\sim 2 \text{ km}$ upstream from Atenquique village. In MC, the flow reaches the site in $[600, 900] \text{ s}$, with a flow height of initially $[5, 7] \text{ m}$, and $[3, 5] \text{ m}$ at $t_f = 2400 \text{ s}$. Flow speed is initially in $[1.5, 4.5] \text{ m/s}$, and one-third of these values are at t_f . Only the basal friction can be dominant, with gravitational force being 40% of it, and internal friction 25%, on average. In PF the flow reaches the site at $[300, 1000] \text{ s}$, with an initial flow height of $[4, 8] \text{ m}$, having a short-lasting peak of 10 m in the 95th percentile, and $[3, 5] \text{ m}$ at t_f . Flow speed is initially in $[4, 6] \text{ m/s}$, and has a short
30 peak of almost 14 m/s in the 95th percentile. It becomes $[2.0, 2.5] \text{ m/s}$ at t_f . Either basal friction, gravity, or pressure force (related to the gradient of thickness) can be dominant. Gravitational force adds 80% of the expected contribution, while basal friction 70% and pressure force 45%. In VS, the flow first reaches the site in $[300, 800] \text{ s}$, with a flow height of $[1.5, 12] \text{ m}$, initially, and a short peak at 14 m, becoming $[1.5, 5] \text{ m}$ at t_f . Flow speed is in $[1, 15] \text{ m/s}$, initially, has a short peak at 20 m/s , and then becomes $[1.5, 3.5] \text{ m/s}$ at t_f . Either basal friction or gravity can be dominant, both with 75% expected contribution.



We note that gravity tends to slightly decrease in expected contribution, as well as its dominance factor, through time. This is a numerical effect related to the variation of the mesh, which changes our approximation of local slope.

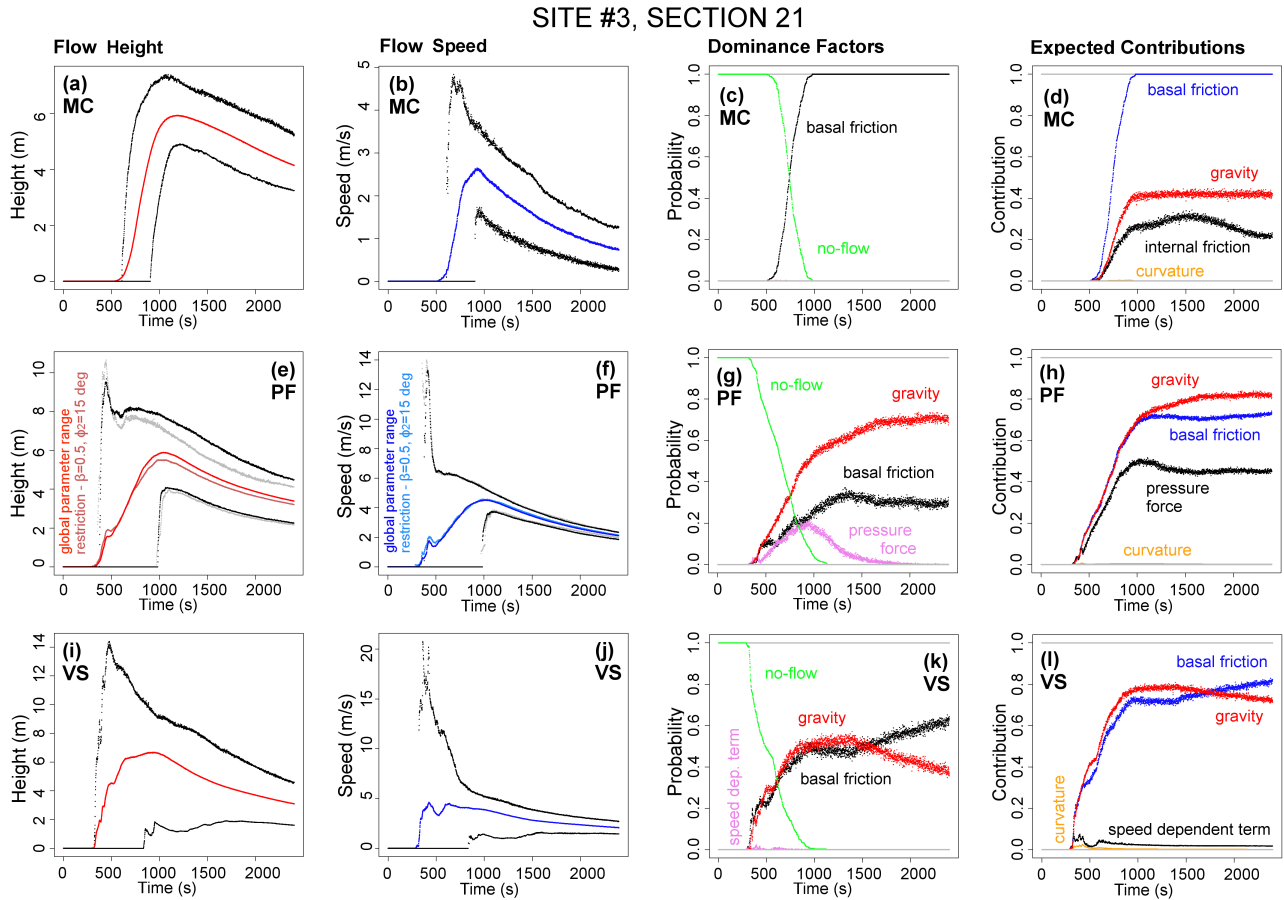


Figure 8. Local flow properties in Site #3, ~2 km upstream from Atenuique village. (a,e,i) show flow height, (b,f,j) flow speed, (c,g,k) dominance factors, (d,h,l) expected contributions of the force terms. Different models are plotted separately: (a-d) assume MC; (e-h) assume PF, and (e,f) include estimates on a hyperplanar restriction of the input domain; (i-l) assume VS. In (a,b,e,f,i,j) colored line is mean value, black/gray lines are 5th and 95th percentile bounds.

In summary, MC is characterized by a lower speed, and by the dominance of basal friction. The expected contribution of the internal friction is not negligible, meaning the internal shear of the material is important. In PF, the pressure force contribution is significant, and it can even be the dominant force initially. This is related to the steepening of the flow front. An initial short lasting wave of high speed is observed in either PF or VS, as is particularly evident in the upper bound of the plots. This fast wave is related to the closest source, #3. The uncertainty affecting height and speed is generally higher in VS than in PF, in spite of the higher dimensionality of the second.



Figure 9 shows the local properties at site #4, located immediately upstream from Atenquique village, and close to the supports of the new bridge of the freeway to the city of Colima. In MC, the flow reaches the site in [1300, 2100] s, with a flow height of [2, 5.5] m. Flow speed is < 0.6 m/s, and 0.1 m/s, on average. Only basal friction is dominant, with the gravitational force being 30% of basal friction, and internal friction 10%, on average. In PF, the flow reaches the site at [600, 1800] s, with a flow height of [3, 6] m, which is stable in time. Flow speed is initially in [1, 4] m/s and half of these values are at t_f . Either basal friction or gravity can be dominant. Gravitational force can be 95% of the expected contribution, while basal friction is 65%, and the pressure force, 25%.

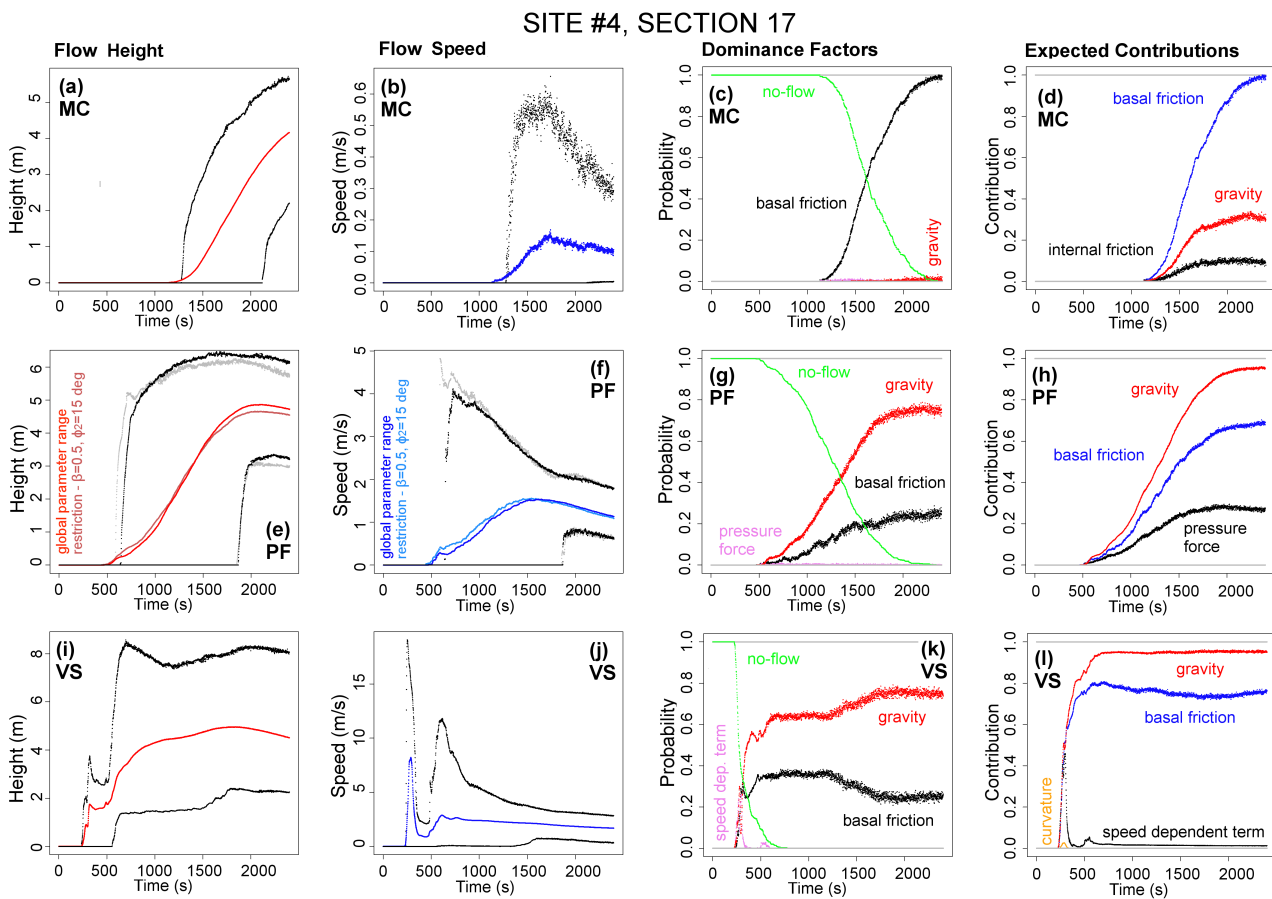


Figure 9. Local flow properties in Site #4, immediately before Atenquique village. (a,e,i) show flow height, (b,f,j) flow speed, (c,g,k) dominance factors, (d,h,l) expected contributions of the force terms. Different models are plotted separately: (a-d) assume MC; (e-h) assume PF, and (e,f) include estimates on a hyperplanar restriction of the input domain; (i-l) assume VS. In (a,b,e,f,i,j) colored line is mean value, black/gray lines are 5th and 95th percentile bounds.

In VS, the flow reaches the site in [250, 550] s, with a first wave of < 3 m. A second wave of [1.5, 8] m arrives, and stays stable in depth. Flow speed also shows two waves - it is < 19 m/s, initially, then rises to < 12 m/s, with a gap in the



middle. It is $[1, 3] \text{ m/s}$ at t_f . Either gravity or basal friction can be dominant, with 95% and 80% of the expected contribution, respectively. In the initial fast wave, the speed dependent friction can be dominant, with 25% of the expected contribution.

In summary, all the models show lower flow height and speed than at the previous site upstream. The flow depth is stable, without decreasing downstream, meaning no formation of a significant deposit. MC is much slower than the other models, and its dynamics is completely dominated by basal friction. An initial, short-lasting wave of high speed is observed in VS. This fast wave is related to source #5 in Arroyo Platános.

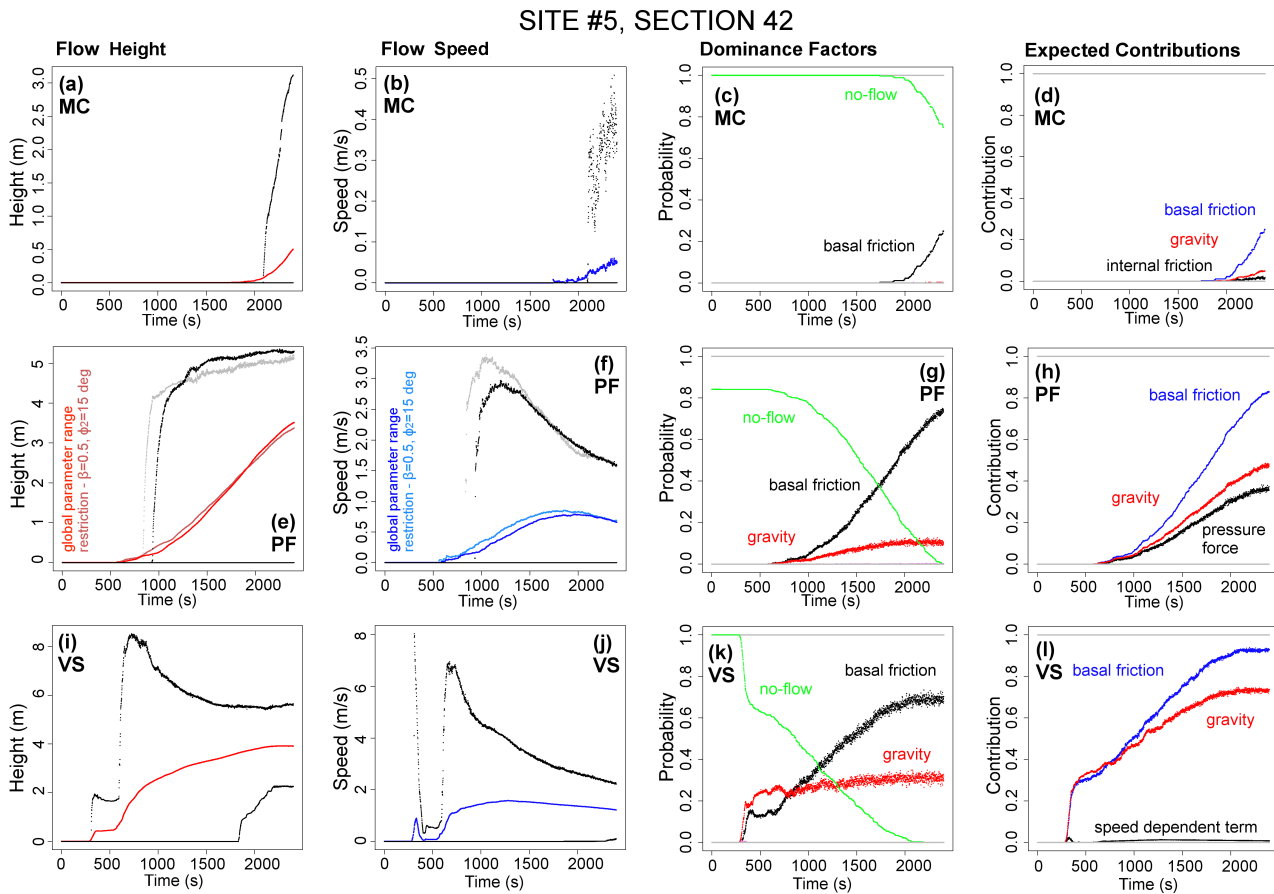


Figure 10. Local flow properties in Site #5, ~ 1 km downstream inside Atenquique village. (a,e,i) show flow height, (b,f,j) flow speed, (c,g,k) dominance factors, (d,h,l) expected contributions of the force terms. Different models are plotted separately: (a-d) assume MC; (e-h) assume PF, and (e,f) include estimates on a hyperplanar restriction of the input domain; (i-l) assume VS. In (a,b,e,f,i,j) colored line is mean value, black/gray lines are 5th and 95th percentile bounds.

Figure 10 shows the local properties at site #5, ~ 1 km downstream from site #4, inside the bounds of Atenquique village. In MC, the flow only starts to inundate the site after 2100 s, with a flow height < 3 m. Flow speed is $< 0.5 \text{ m/s}$, and ten times lower on average. Only basal friction can be dominant. In PF, the flow reaches the site at $[900, 2400]$ s, with a flow height



< 5 m. Flow speed is initially < 3 m/s, and less than half of this value at t_f . Basal friction dominates the dynamics, with 45% expected contribution from the gravitational force, and 35% from the pressure force. In VS, the flow reaches the site in [300, 600] s, with a first wave of < 2 m, and then a second wave < 8 m. This second wave becomes [2, 5.5] m at t_f . Flow speed is < 8 m/s in the first wave, and then < 7 m/s in the second, with a gap in the middle. The average speed is stable at 1.5 m/s. Either basal friction or gravity can dominate, with 95% and 70% expected contributions, respectively.

In summary, the models show a decrease in flow height and speed compared to the previous site. In MC, the site is not always reached, and in PF some input values inundate the site only at the end of the time domain. In PF, restriction of the inputs over a lower dimensional subspace produces a lag of about 100 s, possibly motivated by a fixed value of $\phi_2 = 15^\circ$ being higher than the middle of its variable range. The fast wave in VS is again related to source #5.

5 The likelihood of a model given uncertain data

Figures 11 and 12 show the flow height and speed histograms at the three selected sites, either their maximum value, or their value at $t = 2400$ s. These confirm what is summarized in the previous section. The following probability density values are evaluated with respect to m and m/s, respectively. In Figure 11:

- **Site #3** Flow height pdf at t_f is above 0.1 over: [3, 5.5] m in MC, [2, 4.5] m in PF and [1.5, 4.5] m in VS. The first two models are more peaked, while the third produces a tail of very large thickness values, up to 8 m. The maximum height pdf is above 0.1 over: [5.5, 8] m in MC, [6, 9] m in PF, [8, 13] in VS.
- **Site #4** Flow height pdf at t_f is above 0.1 over: [2.5, 6] m in MC, [3, 6] m in PF and [2, 7] m in VS. The maximum height pdf is above 0.1 over: [2.25, 6] m in MC, [5, 7] m in PF, [6, 9.5] m in VS. The three models show well separate modal values at 4, 6 and 8 m, respectively.
- **Site #5** In MC and PF do not always reach the site in $T = [0, 2400]$ s, so they both show a modal value of flow height in 0 m. The flow height pdf at t_f is above 0.1 over: [1, 1.5] m in MC with a tail up to 3.5 m, [3, 5.5] m in PF, [2, 6] m in VS. The maximum height pdf is almost equal to final height in MC, and it is above 0.1 over: [3.5, 6] m in PF, [3.5, 9] m in VS. Both PF and VS show a modal value at 5 m.

In Figure 12:

- **Site #3** Flow speed pdf at t_f is above 0.25 over: [0.1, 1.4] m/s in MC, [1.6, 2.4] m/s in PF and [1.4, 2.8] m/s in VS. MC is bimodal at 0.5 m/s and 1 m/s, while PF has a modal value at 2.1 m/s. The maximum speed pdf is above 0.05 over: [1, 7] m/s in MC, [4, 8] m in PF, [4, 16] in VS. PF and VS have tails up to 25–30 m/s.
- **Site #4** Flow speed pdf at t_f is above 0.25 over: [0.00, 0.45] m/s in MC, [0.6, 1.8] m/s in PF and [0.5, 3.0] m/s in VS. PF has a modal value at 1 m/s. Maximum speed pdf in MC is concentrated below 1 m/s. In PF, it is above 0.25 over [1, 5] m/s. In VS, it is bimodal and above 0.25 over: [2, 6] m/s and [12, 20] m/s.



HISTOGRAMS OF LOCAL FLOW HEIGHT

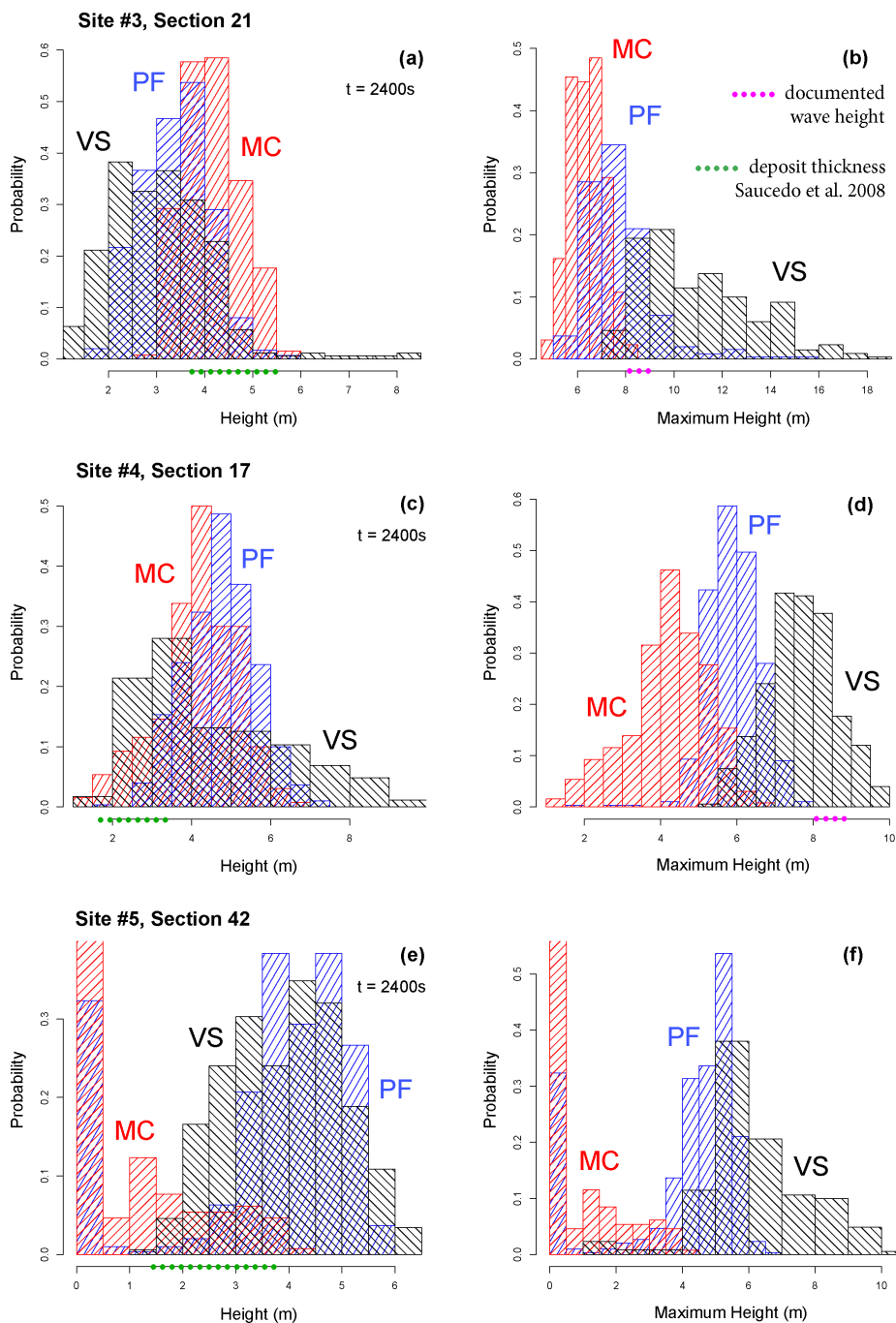


Figure 11. Histograms of local flow height in Sites #3,#4, #5. (a,c,e) show height at $t = 2400$ s, (b,d,f) maximum height. Different models are displayed with different colors. Dots on the height axis show the uncertainty interval of data - green is the deposit thickness of Saucedo et al. (2008) and unpublished data, violet is the wave height documented by the survivors.



HISTOGRAMS OF LOCAL FLOW SPEED

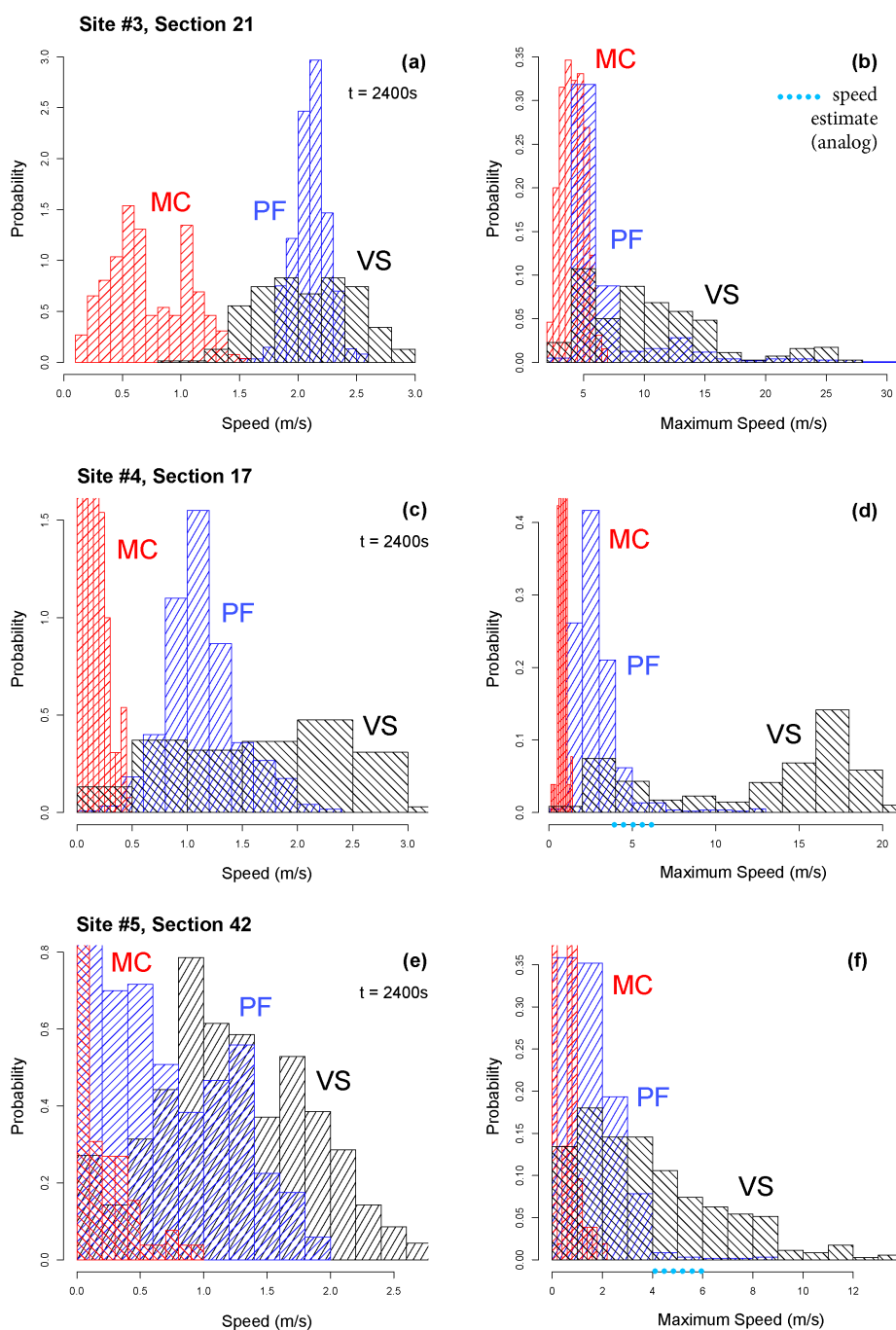


Figure 12. Histograms of local flow speed in Sites #3,#4, #5. (a,c,e) show speed at $t = 2400 s$, (b,d,f) maximum speed. Different models are displayed with different colors. Cyan dots on the speed axis show the uncertainty interval of estimated speed Pierson (1985).



- **Site #5** Flow speed pdf at t_f is above 0.25 over: [0.0, 0.4] m/s in MC, [0.0, 1.4] m/s in PF and over [0.0, 0.2] and [0.4, 2.2] m/s in VS. The maximum speed pdf is above 0.05 over: [0.0, 0.2] and [0.4, 1.2] m/s in MC, to [0, 4] m in PF, [0, 9] in VS. PF and VS have tails up to 8 and 13 m/s, respectively.

5.1 Alternative performance scores of the models

- 5 In Figures 11 and 12, we display the empirical data concerning the observed quantities. These intervals are examples of uncertain data to test our methodology. Further research could refine/modify them.

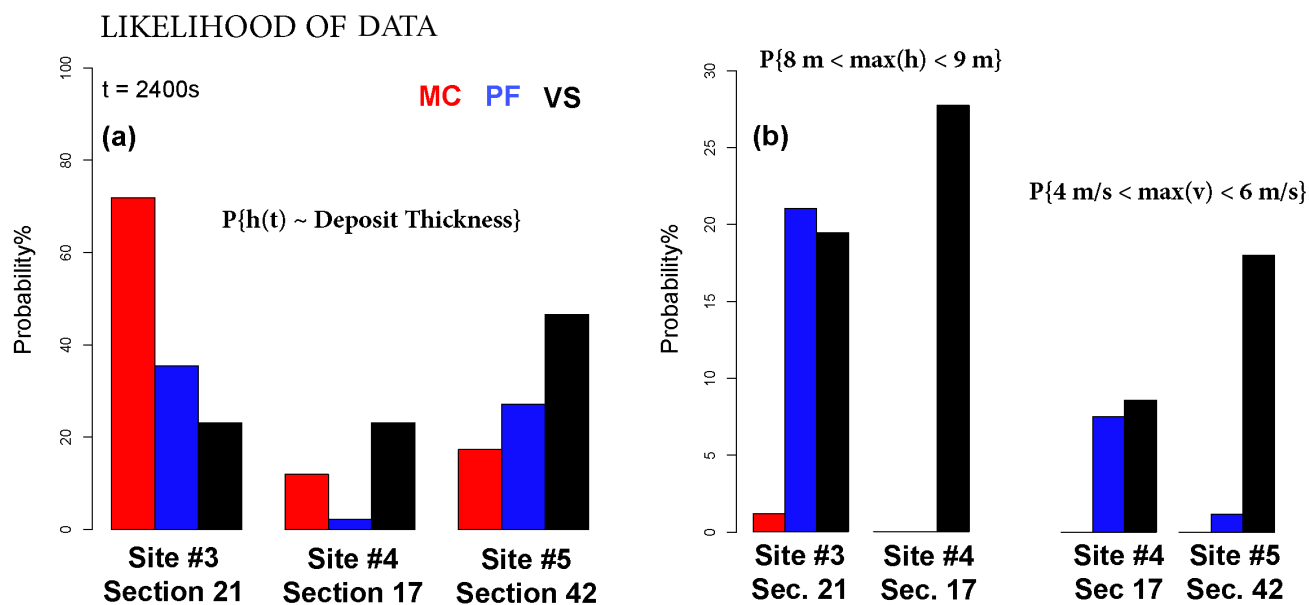


Figure 13. Barplots of data likelihood in Sites #3, #4, #5. (a) compares flow height at $t = 2400$ s with observed deposit thickness (Saucedo et al., 2008). (b) compares maximum height and maximum speed with observed wave height (Ponce-Segura, 1983) and analog flow speed (Pierson, 1985). Different models are displayed with different colors.

1. The deposit thickness, calculated from the envelope of the closest field sections, is [3.7, 5.5] m at **Site #3**, [1.7, 3] m at **Site #4**, and [1.4, 3.8] m at **Site #5** (Saucedo et al., 2008).
2. the flow height in Atenquique village, from historical documents and witnesses, is [8, 9] m at **Site #3** and/or **Site #4** (Ponce-Segura, 1983; Saucedo et al., 2008).
3. The flow speed following the inundation of the village, based on a comparison with analog flows, is [4, 6] m/s at **Site #4** and/or **Site #5** (Pierson, 1985; Saucedo et al., 2008).



The estimation of the likelihood of the pieces of observed data is an essential step towards the definition of partial solutions of the inverse problem. Besides this, it is also relevant information in the model selection problem. The likelihood of a data piece, D_i , attaining its value given a certain model is defined as $P^j(D_i), \forall i \in I, \forall M_j \in \mathcal{M}$. We remark that this is not a pdf value, but the probability of a measurable set. Figure 13 shows the barplots of data likelihood. Figure 13a considers deposit thickness values, under the assumption that they are equivalent to the flow height at t_f . At Site #3, 70% of MC inputs provide flow thickness consistent with the deposit range, against 35% of PF and 20% of VS inputs. At Site #4, likelihood scores are lower: 20% in MC, 10% in VS, <5% in PF. At Site #5, instead, we have: 15% in MC, 25% in PF, 45% in VS. Figure 13b evaluates the maximum flow height when the flow entered Atenquique village. In Site #3, 20% of inputs in PF and VS provide results consistent with data, while only <5% do so in MC. At Site #4, the likelihood score of VS is 27%, while it is null in the other models. Figure 13c focuses on the maximum flow speed after the flow inundated the village. At Site #4, 8% of inputs in PF and 9% in VS provide speeds in the most likely range. At Site #5, these are only 1% in PF, and 17% in VS.

In summary, model performance is dependent on the selected quantity of interest, and on the spatial location. Regarding the deposits, MC performs well at Site #3, while VS does so at Site #5. In the evaluation of the maximum flow depth in the village, both PF and VS can replicate the values at Site #3, and only VS can replicate the values at Site #4. If we focus on the maximum flow speed, at Site #4 both PF and VS perform moderately well, while at Site #5, only VS can provide speed values inside the assumed range.

6 Partial solutions in the input space

Figures 14, 15, 16 display three examples of partial solutions in the specialized experimental design. For each example $n = 1, 2, 3$ we select a subfamily of empirical data $(D_i)_{i \in I_n}$ and define, $\forall j$:

$$\tilde{\Theta}_n^j := \bigcap_{i \in I_n} \Omega_i^j. \quad (6)$$

Example #1 focuses on the deposit thickness data at Sites #3, #4, #5. Examples #2 and #3 consider the deposit thickness at Site #5 only. Additionally, Example #2 evaluates the maximum flow height at Site #4, and the maximum flow speed at Site #5, while Example #3 does that at Site #3 and Site #4, respectively.

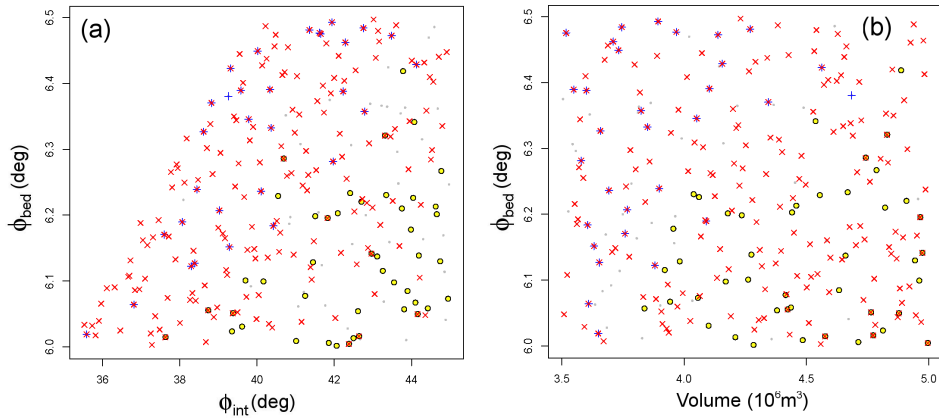
Figure 14 concerns Example #1. In all the models, $\tilde{\Theta}_1^j = \emptyset$. In MC, the set of inputs that replicate the deposit thickness at Site #4 are disjoint from those in Site #5. Instead, in PF and VS the inputs related to Site #3 are disjoint from those related to Site #4. Figure 15 concerns Example #2. In MC and PF, the maximum flow height from the data is never reproduced. In MC, the required maximum flow speed is never achieved. Thus, $\tilde{\Theta}_2^j \neq \emptyset$ only if $j = \text{VS}$. The partial solution inputs in $\tilde{\Theta}_2^{\text{VS}}$ are bounded by:

$$\arctan(\mu) \in [1.0, 1.8], \quad \xi \in [3.1, 3.7], \quad V \in [3.8, 5.0] \times 10^6 \text{ m}^3.$$



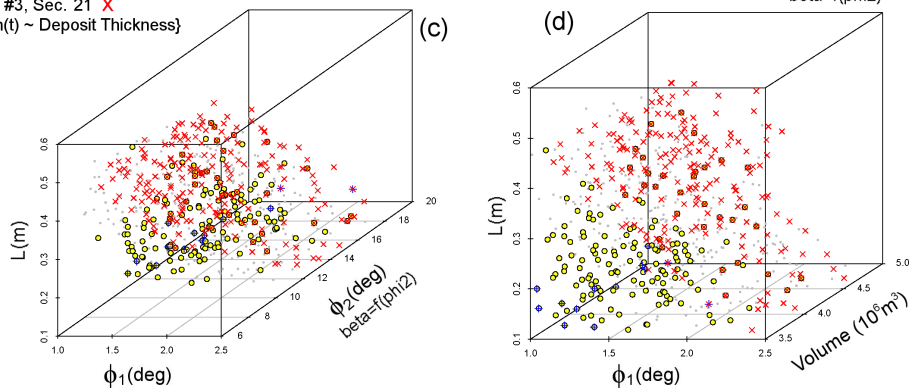
PARTIAL SOLUTIONS SUBDESIGN, EXAMPLE #1

MOHR-COULOMB LHS (260 points)



Site #5, Sec. 42 ●
 Site #4, Sec. 17 +
 Site #3, Sec. 21 ×
 {h(t) ~ Deposit Thickness}

POULIQUEN-FORTERRE LHS (600 points)



VOELLMY-SALM LHS (350 points)

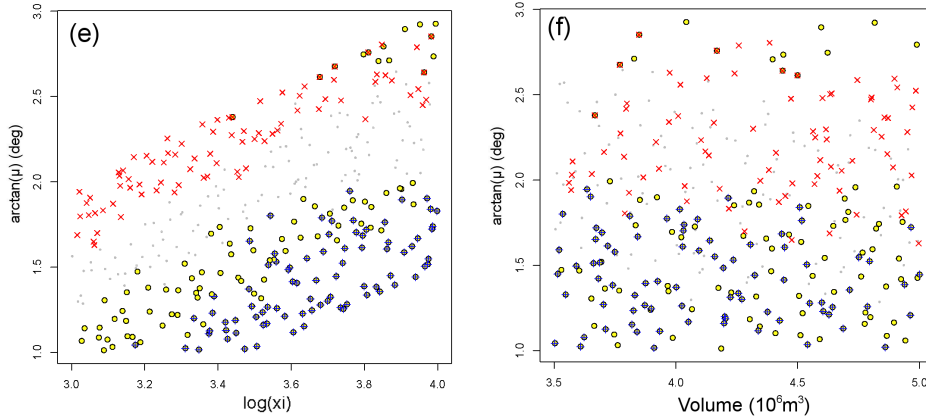
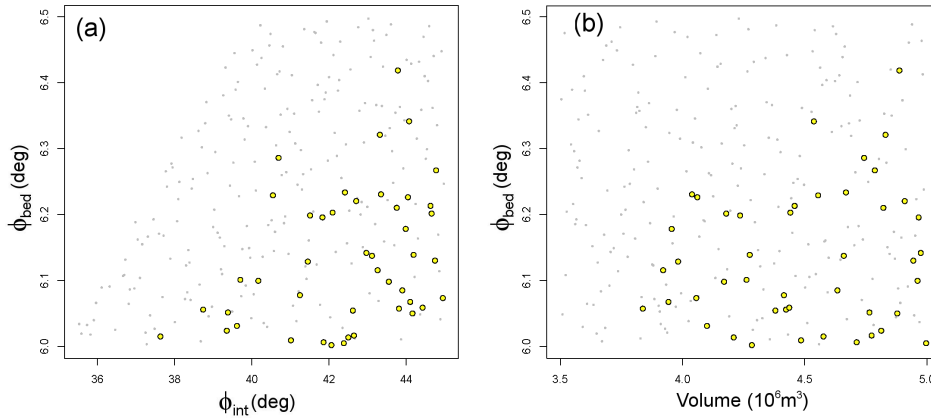


Figure 14. Example #1 of partial solution inputs in (a-b) MC, (c-d) PF, (e-f) VS experimental design. (a-c-e) are projected along the V coordinate, and (b-d-f) along ϕ_{int} , ϕ_2 and ξ coordinates, respectively. The color expresses the considered data: yellow is deposit thickness in Site #5, blue in Site #4, red in Site #3 (Saucedo et al., 2008).



PARTIAL SOLUTIONS SUBDESIGN, EXAMPLE #2

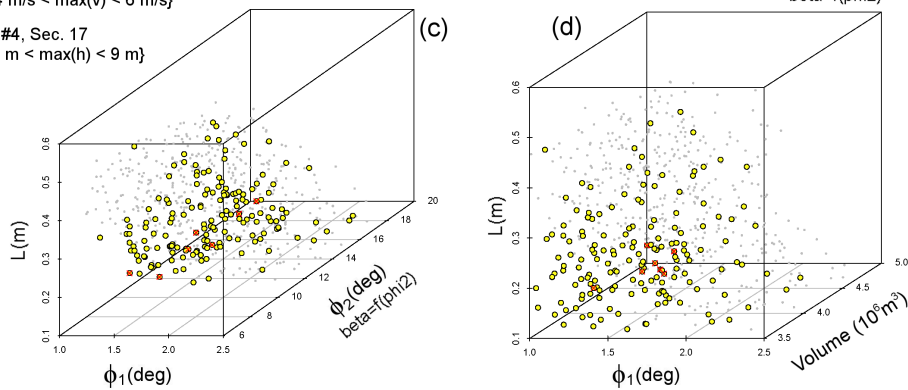
MOHR-COULOMB LHS (260 points)



Site #5, Sec. 42
 ● {h(t) ~ Deposit Thickness}
 × {4 m/s < max(v) < 6 m/s}

Site #4, Sec. 17
 + {8 m < max(h) < 9 m}

POULIQUEN-FORTERRE LHS (600 points)



VOELLMY-SALM LHS (350 points)

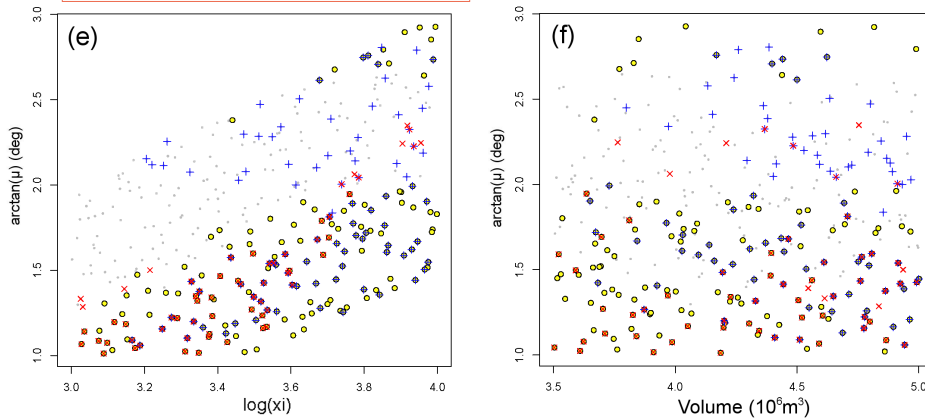
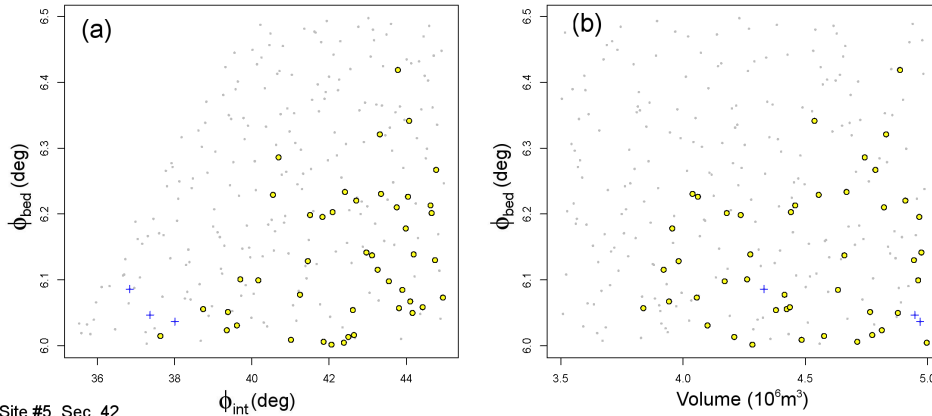


Figure 15. Example #2 of partial solution inputs in (a-b) MC, (c-d) PF, (e-f) VS experimental design. (a-c-e) are projected along the V coordinate, and (b-d-f) along ϕ_{int} , ϕ_2 and ξ coordinates, respectively. The color expresses the considered data: yellow is deposit thickness in Site #5 (Saucedo et al., 2008), blue is wave height in Site #4 (Ponce-Segura, 1983), red is flow speed in Site #5 (Pierson, 1985).



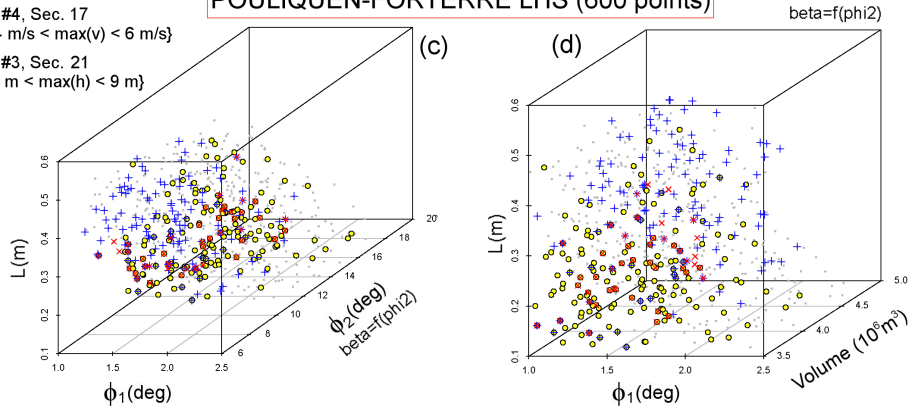
PARTIAL SOLUTIONS SUBDESIGN, EXAMPLE #3

MOHR-COULOMB LHS (260 points)



- Site #5, Sec. 42
● {h(t) ~ Deposit Thickness}
- Site #4, Sec. 17
× {4 m/s < max(v) < 6 m/s}
- Site #3, Sec. 21
+ {8 m < max(h) < 9 m}

POULIQUEN-FORTERRE LHS (600 points)



VOELLMY-SALM LHS (350 points)

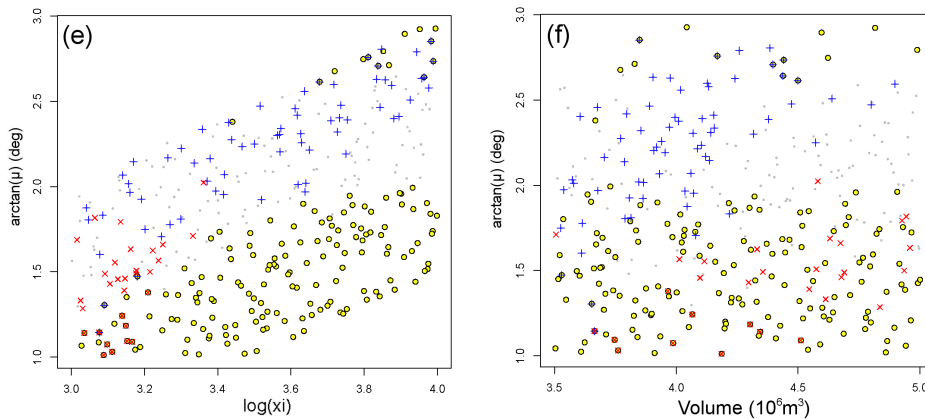


Figure 16. Example #3 of partial solution inputs in (a-b) MC, (c-d) PF, (e-f) VS experimental design. (a-c-e) are projected along the V coordinate, and (b-d-f) along ϕ_{int} , ϕ_2 and ξ coordinates, respectively. The color expresses the considered data: yellow is deposit thickness in Site #5 (Saucedo et al., 2008), blue is wave height in Site #3 (Ponce-Segura, 1983), red is flow speed in Site #4 (Pierson, 1985).



Figure 16 is related to Example #3. In MC, the required maximum flow speed from the data is never reproduced. We have that $\tilde{\Theta}_2^j \neq \emptyset$ for $j \in \{\text{PF}, \text{VS}\}$. In PF, the partial solution inputs in $\tilde{\Theta}_3^{\text{PF}}$ are bounded by:

$$\phi_1 \in [1.0, 1.6], \quad L \in [0.12, 0.25] \text{ m}, \quad V \in [3.9, 4.9] \times 10^6 \text{ m}^3.$$

In VS, only one point belongs to the partial solution input set, with $\arctan(\mu) \simeq 1.2$, $\xi \simeq 3.1$, $V \simeq 3.6 \times 10^6 \text{ m}^3$. Remarkably, the input spaces reproducing the three required pieces of empirical data are almost disjoint in pairs, and $\tilde{\Theta}_3^{\text{VS}}$ is small and close to the frontiers of the uncertainty ranges. Additional details in PF over the hyperplane $\{\beta = 0.5, \phi_2 = 15\}$ described in Table 1 are included in Supporting Information SI6.

5 6.1 Examples of conditional results

The solution of the partial inverse problems can enable us to select a model, which nevertheless depends on the required properties and the spatial location. In particular:

- in Example #1 the inverse problem is not well posed,
- in Example #2 only in VS can we find solutions: $\tilde{\Theta}_2^{\text{VS}} \neq \emptyset$,
- 10 – in Example #3 both in PF and VS we find solutions: $\tilde{\Theta}_3^{\text{PF}} \neq \emptyset$, $\tilde{\Theta}_3^{\text{VS}} \neq \emptyset$.

The points in the experimental design that belong to $\tilde{\Theta}_2^{\text{VS}}$ and $\tilde{\Theta}_3^{\text{PF}}$ are 21 and 9 respectively. We do not detail $\tilde{\Theta}_3^{\text{VS}}$ because it contains only one design point and the results can be disrupted even by relatively small variations of the inputs. Additional tests at a finer resolution in the experimental design could be performed to achieve a more accurate characterization of the conditional input spaces, if required.

In Figures 17 and 18, we report the histograms of:

$$K = \max_{t \in T} \kappa, \quad \kappa_f := \kappa(t_f) \quad Q := \max_{t \in T} \frac{\kappa}{h}$$

- 15 at Sites #4 and #5. The spatial maps of the maximum in flow height, h , and kinetic energy, κ , are also displayed. The *dynamic pressure* Q and the *kinetic energy* κ formally assume a mass with unit density.

In Figure 17, at Site #4:

$$K \in [100, 400] \text{ m}^3/\text{s}^2, \quad \kappa_f \in [4, 16] \text{ m}^3/\text{s}^2, \quad Q \in [0, 150] \text{ m}^2/\text{s}^2$$

and at Site #5:

$$K \in [40, 140] \text{ m}^3/\text{s}^2, \quad \kappa_f \in [0, 9] \text{ m}^3/\text{s}^2, \quad Q \in [7.5, 17.5] \text{ m}^2/\text{s}^2$$

The modal values of K are $\sim 225 \text{ m}^3/\text{s}^2$ and $60 \text{ m}^3/\text{s}^2$, respectively.



CONDITIONAL RESULTS - VOELLMY SALM

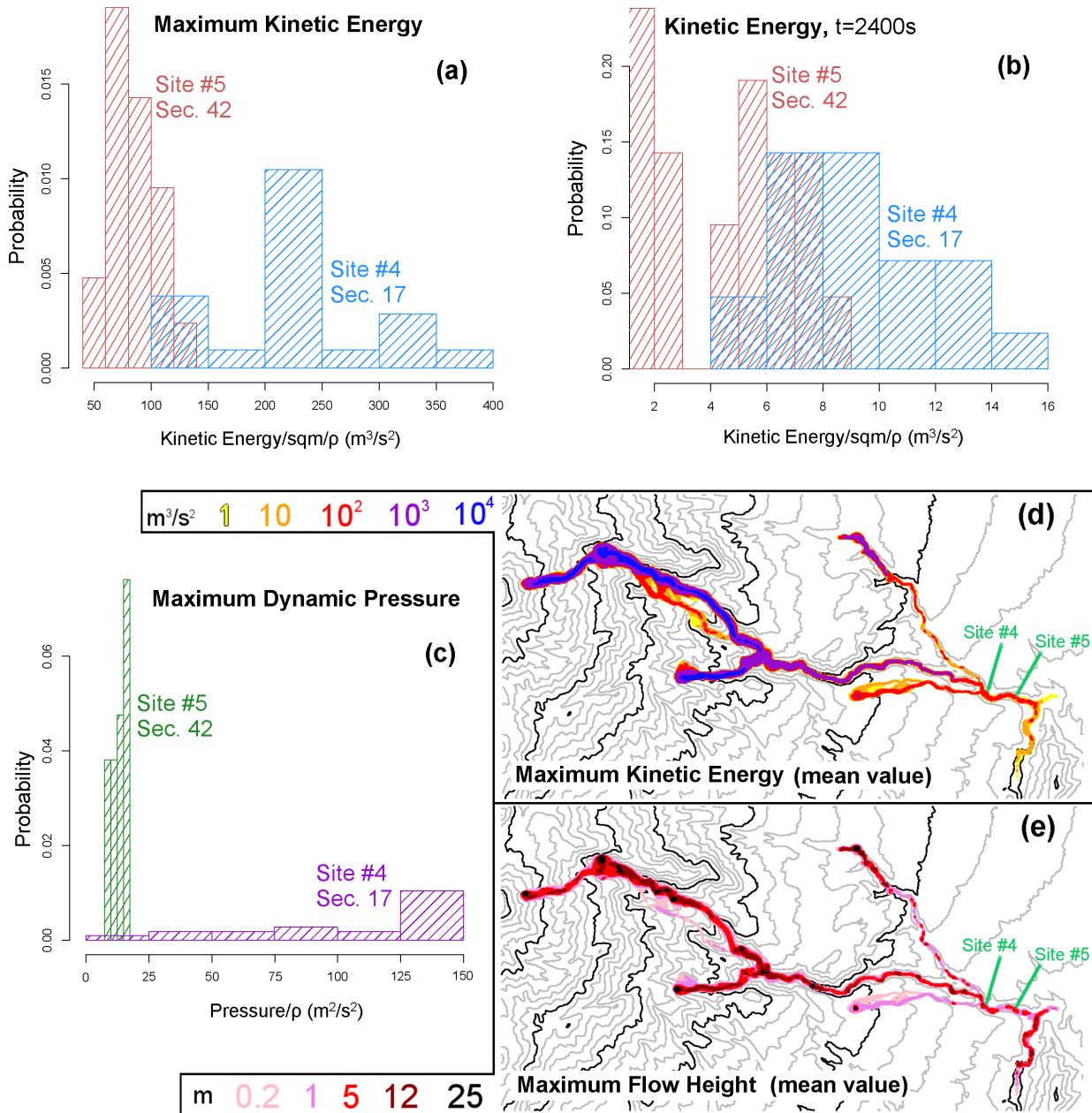


Figure 17. Flow properties of VS model, over the input space $\tilde{\Theta}_2^{VS}$. Histograms of (a,b) local kinetic energy and (c) dynamic pressure in Sites #4 and #5, (a) at $t = 2400$ s, (b,c) maximum value. Different sites are displayed with different colors. Mean values over $\tilde{\Theta}_2^{VS}$ of the maps of maximum (d) kinetic energy and (e) flow height as a function of time. Colors are related to their values. Elevation contours are included at intervals of 100 m (gray) and 500 m (black) (NASA (JPL), 2014). Sites #4 and #5 are displayed.



CONDITIONAL RESULTS - POULIQUEN FORTERRE

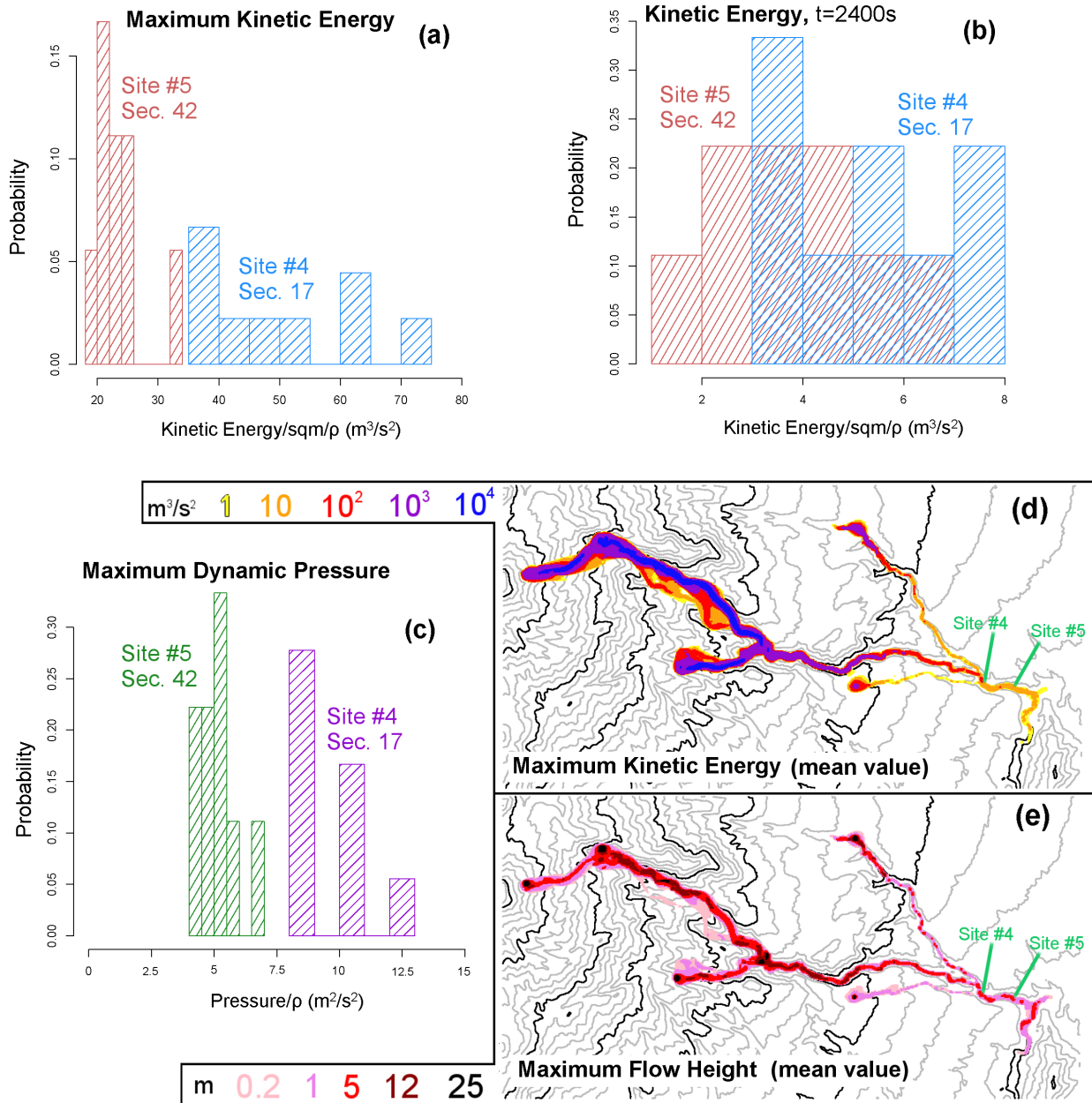


Figure 18. Flow properties of PF model, over the input space $\tilde{\Theta}_3^{\text{PF}}$. Histograms of (a,b) local kinetic energy and (c) dynamic pressure in Sites #4 and #5, (a) at $t = 2400$ s, (b,c) maximum value. Different sites are displayed with different colors. Mean values over $\tilde{\Theta}_3^{\text{PF}}$ of the maps of maximum (d) kinetic energy and (e) flow height as a function of time. Colors are related to their values. Elevation contours are included at intervals of 100 m (gray) and 500 m (black) (NASA (JPL), 2014). Sites #4 and #5 are displayed.



In Figure 18, at Site #4:

$$K \in [35, 75] \text{ m}^3/\text{s}^2, \quad \kappa_f \in [3, 8] \text{ m}^3/\text{s}^2, \quad Q \in [8, 13] \text{ m}^2/\text{s}^2$$

and at Site #5:

$$K \in [18, 34] \text{ m}^3/\text{s}^2, \quad \kappa_f \in [1, 7] \text{ m}^3/\text{s}^2, \quad Q \in [4, 7] \text{ m}^2/\text{s}^2$$

Modal values are not well-constrained in this case.

In the spatial maps, PF shows slightly lower maximum flow height, and significantly lower energy than VS, especially in the distal part of the domain. The flow in the tributaries can reach the village, except for the smallest flows of Arroyo Plátanos in PF, which however at t_f are only tens of meters from the main branch. As in the unconditional maps, local maxima of flow height are located in the ravine, while the kinetic energy shows a more regular decrease.

In summary, the statistical analysis of the partial solutions told us:

- the deposit thickness in the three selected sites is not reproduced by any of the models. In particular, the input choices that fit the Site #3 are inconsistent with those that fit the deposit downstream. This advocates the possibility of testing additional models, for example including an entrainment term in the mass conservation equation.
- MC model is not capable of reproducing the required maximum flow height and speed in the village. Its feasible input space does not allow us to reduce the friction further. Even if PF can reproduce the required height and speed when impacting the village, only VS is capable of maintain those values also in the downstream part of the village.

In particular, models using MC based rheologies are unlikely to reproduce the properties of the 1955 flow. Instead, the flexible basal friction angle in PF allows for both higher speed and longer runout, consistent with those observed. The higher dimensionality of its parameter space is not significantly increasing the uncertainty affecting the outputs. Similarly, the velocity dependent term in VS is a very robust mechanism for preserving numerical stability, avoiding the spurious results that affect the MC model at equivalently low values of basal friction. Indeed the most high levels of simulated speed are observed with VS.

We remark that the assumed $[4, 6] \text{ m/s}$ constraint on the maximum flow speed has an immediate effect on the dynamic pressure estimates. Imposing it at Site #5 as in the Example #2, or Site #4 as in the Example #3, can radically change the results, even if the required deposit thickness at Site #5 is not modified. Additional information on the speed properties in the village could thus allow us to further discriminate the performance of the models.

7 Conclusions

In this study, we have introduced a new prediction-oriented method for hazard assessment of volcaniclastic debris flows (lahars), based on multiple geophysical mass flow models. Similar strategies have been applied in hurricane hazard analysis (Krishnamurti et al., 2016; Ghosh and Krishnamurti, 2018). In particular, our approach decomposes the original inverse problem into a hierarchy of simpler problems, and allows for the exploration of the impact of synthetic flows that are similar to those that occurred in the past, but different in plausible ways.



We applied our procedure to a case study of the 1955 Atenuique volcanoclastic debris flow. We adopted and compared three depth averaged models based on the Saint-Venant equations that are widely used in hazard assessment. Namely, Mohr-Coulomb (MC), Pouliquen-Forterre (PF), and Voellmy-Salm (VS). In summary:

- We defined a *specialized experimental design* after assuming: the realism of the underlying physics, the numerical simulation is robust in some sense, and the flow dynamics or inundation output is meaningful. This produced a range of output simulations that contain valuable information for hazard assessment.

Indeed, these outputs do not strictly reconstruct past flows, hence can provide hazard estimates under constraints weaker than those used therein, potentially including cases of extreme events. Moreover, our designs were not trivial geometrically, due to the correlated effects of model inputs. This is a first step towards the development of an objective and partially automated experimental design.

- We described the statistics of the outputs and contributing variables by performing a Monte Carlo simulation over the specialized design. We made global maps of the flows, and investigated detailed characteristics. This allowed us to calculate the likelihood that different model realizations reasonably represented the 1955 Atenuique flow, given multiple pieces of field data regarding its characteristics. Depending on how it is looked at, the exercise provided useful information in either model selection or data inversion.

Our analysis concerned the mean values and uncertainty percentiles of quantities of interest. Moreover, the probabilistic setting allowed us to make inferences regarding the uncertainty affecting the data. We analyzed the contributing variables, which shed light on the different assumptions underlying the three considered models. In particular, the MC model is generally characterized by a lower speed over its feasible input space, when compared to the other models. The expected contribution of the internal friction is significant, meaning the internal shear of the material is important. In the PF model, the pressure force contribution related to the steepening of the flow front was locally significant, and was sometimes even the dominant force. An initial, short-lasting wave of high speed related to the closest of the multiple sources was observed in both PF and VS. The uncertainty in height and speed was generally higher in VS than in PF, in spite of the higher dimensionality of the second.

- We constructed partial solutions to the inverse problem, conditioning the specialized experimental design to be consistent with subsets of the observed data. We described the corresponding inputs sets, and investigated their intersection. We found model selection to be inherently linked to the inversion problem. That is, the partial inverse problems enabled us to select models depending on the example characteristics and spatial location.

In particular, when attempting to correctly represent the deposits, MC performed well about 2 km upstream from the village, while VS did so in the village. In the evaluation of the maximum flow or run-up depth, both PF and VS replicated the values 2 km upstream from Atenuique, but only VS replicated the values in the village. In terms of maximum flow speed, both PF and VS performed moderately well in the village, but only VS performed well 1 km downstream. These results are consistent with evolution of flow rheology downstream in the vicinity of the village, from MC above the



village, to either PF or VS within and downstream from the village. If VS was dominant as the flow propagated downstream, the meaning here may reflect an evolution from inertial to macroviscous debris flow behavior near Atenquique, perhaps related to engulfment of the reservoir just upstream from the village.

The connection of inverse problems and model uncertainty represents a fundamental challenge in the future development of multi-model solvers, suggesting as it does the advantages of dynamically selecting the model based on performance against local data for previous, example flows and their deposits.

Code and data availability. Datasets are available from references and Supporting Information. The 4th release of TITAN2D is available from vhub.org.

Appendix A: Overview of the depth-averaged models

Many models based on different assumptions from those adopted in this study are available in literature, either more complex (Pitman and Le, 2005; Iverson and George, 2014) or more simple (Dade and Huppert, 1998). We decided to focus on these three because of their historical relevance, and because they are all incorporated in our large scale mass flow simulation framework TITAN2D. We also remark that the poorly constrained data available for the past flow would make the application of a more complex model increasingly difficult.

A1 Mohr-Coulomb

Based on the long history of studies in soil mechanics (Rankine, 1857; Drucker and Prager, 1952), the Mohr-Coulomb rheology (MC) was developed and used to represent the behavior of geophysical mass flows (Savage and Hutter, 1989). Shear and normal stress are assumed to obey Coulomb friction equation, both within the flow and at its boundaries. In other words,

$$\tau = \sigma \tan \phi, \tag{A1}$$

where τ and σ are respectively the shear and normal stresses on failure surfaces, and ϕ is a friction angle. This relationship does not depend on the flow speed.

We can summarize the MC rheology assumptions as:

- *Basal Friction* based on a constant friction angle.
- *Internal Friction* based on a constant friction angle.
- *Earth pressure coefficient* formula depends on the Mohr circle (implicitly depends on the friction angles).
- Velocity based *curvature effects* are included into the equations.



Under the assumption of symmetry of the stress tensor with respect to the z axis, the earth pressure coefficient $k = k_{ap}$ can take on only one of three values $\{0, \pm 1\}$. The material yield criterion is represented by the two straight lines at angles $\pm\phi$ (the internal friction angle) relative to horizontal direction. Similarly, the normal and shear stress at the bed are represented by the line $\tau = -\sigma \tan(\delta)$ where δ is the bed friction angle.

5 A1.1 MC equations

As a result, we can write down the source terms of the Eqs. (1):

$$\begin{aligned} S_x &= g_x h - \frac{\bar{u}}{\|\bar{\mathbf{u}}\|} \left[h \left(g_z + \frac{\bar{u}^2}{r_x} \right) \tan(\phi_{bed}) \right] - h k_{ap} \operatorname{sgn} \left(\frac{\partial \bar{u}}{\partial y} \right) \frac{\partial (g_z h)}{\partial y} \sin(\phi_{int}) \\ S_y &= g_y h - \frac{\bar{v}}{\|\bar{\mathbf{u}}\|} \left[h \left(g_z + \frac{\bar{v}^2}{r_y} \right) \tan(\phi_{bed}) \right] - h k_{ap} \operatorname{sgn} \left(\frac{\partial \bar{v}}{\partial x} \right) \frac{\partial (g_z h)}{\partial x} \sin(\phi_{int}) \end{aligned} \quad (\text{A2})$$

Where, $\bar{\mathbf{u}} = (\bar{u}, \bar{v})$, is the depth-averaged velocity vector, r_x and r_y denote the radii of curvature of the local basal surface. The inverse of the radii of curvature is usually approximated with the partial derivatives of the basal slope, e.g., $1/r_x = \partial \theta_x / \partial x$, where θ_x is the local bed slope.

A2 Pouliquen-Forterre

The scaling properties for granular flows down rough inclined planes led to the development of the Pouliquen-Forterre rheology (PF), assuming a variable frictional behavior as a function of Froude Number and flow depth (Pouliquen, 1999; Forterre and Pouliquen, 2002; Pouliquen and Forterre, 2002; Forterre and Pouliquen, 2003).

PF rheology assumptions can be summarized as:

- *Basal Friction* is based on an interpolation of two different friction angles, based on the flow regime and depth.
- *Internal Friction* is neglected.
- *Earth pressure coefficient* is equal to one.
- Normal stress is modified by a *pressure force* related to the flow thickness gradient.
- Velocity based *curvature effects* are included into the equations.

Two critical slope inclination angles are defined as functions of the flow thickness, namely $\phi_{start}(h)$ and $\phi_{stop}(h)$. The function $\phi_{stop}(h)$ gives the slope angle at which a steady uniform flow leaves a deposit of thickness h , while $\phi_{start}(h)$ is the angle at which a layer of thickness h is mobilized. They define two different basal friction coefficients.

$$\mu_{start}(h) = \tan(\phi_{start}(h)) \quad (\text{A3})$$

$$\mu_{stop}(h) = \tan(\phi_{stop}(h)) \quad (\text{A4})$$

An empirical friction law $\mu_b(\|\bar{\mathbf{u}}\|, h)$ is then defined in the whole range of velocity and thickness. The expression changes depending on two flow regimes, according to a parameter β and the Froude number $Fr = \|\bar{\mathbf{u}}\| / \sqrt{h g_z}$.



A2.1 Dynamic friction regime - $Fr \geq \beta$

$$\mu(h, Fr) = \mu_{stop}(h\beta/Fr) \quad (\text{A5})$$

A2.2 Intermediate friction regime - $0 \leq Fr < \beta$

$$\mu(h, Fr) = \left(\frac{Fr}{\beta}\right)^\gamma [\mu_{stop}(h) - \mu_{start}(h)] + \mu_{start}(h), \quad (\text{A6})$$

5 where γ is the power of extrapolation, assumed equal to 10^{-3} in the sequel (Pouliquen and Forterre, 2002).

The functions μ_{stop} and μ_{start} are defined by:

$$\mu_{stop}(h) = \tan \phi_1 + \frac{\tan \phi_2 - \tan \phi_1}{1 + h/\mathcal{L}} \quad (\text{A7})$$

and

$$\mu_{start}(h) = \tan \phi_3 + \frac{\tan \phi_2 - \tan \phi_1}{1 + h/\mathcal{L}} \quad (\text{A8})$$

10 The critical angles ϕ_1 , ϕ_2 and ϕ_3 and the parameters \mathcal{L}, β are the parameters of the model.

In particular, \mathcal{L} is the characteristic depth of the flow over which a transition between the angles ϕ_1 to ϕ_2 occurs, in the μ_{stop} formula. In practice, if $h \ll \mathcal{L}$, then $\mu_{stop}(h) \approx \tan \phi_2$, and if $h \gg \mathcal{L}$, then $\mu_{stop}(h) \approx \tan \phi_1$.

A2.3 PF equations

The depth-averaged Eqs. (1) source terms thus take the following form:

$$\begin{aligned} 15 \quad S_x &= g_x h - \frac{\bar{u}}{\|\bar{\mathbf{u}}\|} \left[h \left(g_z + \frac{\bar{u}^2}{r_x} \right) \mu_b(\|\bar{\mathbf{u}}\|, h) \right] + g_z h \frac{\partial h}{\partial x} \\ S_y &= g_y h - \frac{\bar{v}}{\|\bar{\mathbf{u}}\|} \left[h \left(g_z + \frac{\bar{v}^2}{r_y} \right) \mu_b(\|\bar{\mathbf{u}}\|, h) \right] + g_z h \frac{\partial h}{\partial y} \end{aligned} \quad (\text{A9})$$

A3 Voellmy-Salm

The theoretical analysis of dense snow avalanches led to the VS rheology (VS) (Voellmy, 1955; Salm et al., 1990; Salm, 1993; Bartelt et al., 1999). Dense snow or debris avalanches consist of mobilized, rapidly flowing ice-snow mixed to debris-
 20 rock granules (Bartelt and McArdell, 2009). The VS rheology assumes a velocity dependent resisting term in addition to the traditional basal friction, ideally capable of including an approximation of the turbulence-generated dissipation. Many experimental and theoretical studies were developed in this framework (Gruber and Bartelt, 2007; Kern et al., 2009; Christen et al., 2010; Fischer et al., 2012). The following relation between shear and normal stresses holds:

$$\tau = \mu\sigma + \frac{\rho\|\mathbf{g}\|}{\xi} \|\bar{\mathbf{u}}\|^2, \quad (\text{A10})$$

25 where, σ denotes the normal stress at the bottom of the fluid layer and $\mathbf{g} = (g_x, g_y, g_z)$ represents the gravity vector. The two parameters of the model are the bed friction coefficient μ and the velocity dependent friction coefficient ξ .

We can summarize VS rheology assumptions as:



- *Basal Friction* is based on a constant coefficient, similarly to the MC rheology.
 - *Internal Friction* is neglected.
 - *Earth pressure coefficient* is equal to one.
 - Additional *turbulent friction* is based on the local velocity by a quadratic expression.
- 5 – Velocity based *curvature effects* are included into the equations, following an alternative formulation.

The effect of the topographic local curvatures is addressed with terms containing the local radii of curvature r_x and r_y . In this case the expression is based on the speed instead of the scalar components of velocity (Pudasaini and Hutter, 2003; Fischer et al., 2012).

A3.1 VS equations

10 Therefore, the final source terms take the following form:

$$\begin{aligned}
 S_x &= g_x h - \frac{\bar{u}}{\|\bar{\mathbf{u}}\|} \left[h \left(g_z + \frac{\|\bar{\mathbf{u}}\|^2}{r_x} \right) \mu + \frac{\|\mathbf{g}\|}{\xi} \|\bar{\mathbf{u}}\|^2 \right], \\
 S_y &= g_y h - \frac{\bar{v}}{\|\bar{\mathbf{u}}\|} \left[h \left(g_z + \frac{\|\bar{\mathbf{u}}\|^2}{r_y} \right) \mu + \frac{\|\mathbf{g}\|}{\xi} \|\bar{\mathbf{u}}\|^2 \right].
 \end{aligned}
 \tag{A11}$$

Appendix B: Contributing variables

Let $[F_n(\mathbf{x}, t)]_{n=1, \dots, N}$ be an array of force terms, where $\mathbf{x} \in \mathbf{R}^d$ is a spatial location, and $t \in T$ is a time instant. The degree
 15 of contribution of those force terms to the flow dynamics can be significantly variable in space and time, and we define the
dominance factors $[p_n(\mathbf{x}, t)]_{n=1, \dots, N}$, i.e., the probability of each $F_n(\mathbf{x}, t)$ to be the dominant force. Those probabilities provide
 insight into the dominance of a particular source or dissipation term on the model dynamics. We remark that we focus on the
 modulus of the forces and hence we cope with scalar terms. It is also important to remark that all the forces depend on the
 input variables, and they can be thus considered as random variables. Furthermore, these definitions are general and could be
 20 applied to any set of contributing variables, and not only to the force terms. More details about this can be found in Patra et al.
 (2018b).

B1 Dominance factors

Let $(F_i)_{i \in I}$ be random variables on $(\Omega, \mathcal{F}, P_M)$. Then, $\forall i$, the dominant variable is defined as:

$$\Phi := \max_i |F_i|.$$



In particular, for each $j \in I$, the dominance factors are defined as:

$$p_j := P_M \{ \Phi = |F_j| \}.$$

Moreover, we define the *random contributions*, an additional tool that we use to compare the different force terms, following a less restrictive approach than the dominance factors. They are obtained dividing the force terms by the dominant force Φ , and hence belong to $[0, 1]$.

B2 Expected contributions

Let $(F_i)_{i \in I}$ be random variables on $(\Omega, \mathcal{F}, P_M)$. Then, $\forall i$, the random contribution is defined as:

$$C_i := \begin{cases} \frac{F_i}{\Phi}, & \text{if } \Phi \neq 0; \\ 0, & \text{otherwise.} \end{cases}$$

5 where Φ is the dominant variable. Thus, $\forall i$, the expected contributions are defined by $E[C_i]$.

In particular, for a particular location x , time t , and parameter sample ω , we have $C_n(\underline{x}, t, \omega) = 0$ if there is no flow or all the forces are null. The expectation of C_n is reduced by the chance of F_n being small compared to the other terms, or by the chance of having no flow in (\underline{x}, t) .

Author contributions. AB and AP conceived the main conceptual ideas. AB implemented and performed the simulations and the statistical
10 analysis. AB wrote the manuscript. AB, AP and MIB interpreted the computational results. All authors discussed the results, commented on the manuscript, provided critical feedback, and gave final approval for publication.

Competing interests. The authors declare that they have no conflict of interest.

Acknowledgements. We would like to acknowledge the support of NSF awards 1339765, 1521855, 1621853 and 1821311. We would like to thank Byron Rupp for his fundamental work on the localization and volume constraints of the Atenuque debris flow (Rupp, 2004), and Ali
15 Akhavan Safaei for the C++ and Python scripts to collect the local outputs and contributing variables on the grid elements (Akhavan-Safaei, 2018).



References

- Aghakhani, H., Dalbey, K., Salac, D., and Patra, A. K.: Heuristic and Eulerian interface capturing approaches for shallow water type flow and application to granular flows, *Computer Methods in Applied Mechanics and Engineering*, 304, 243–264, <https://doi.org/http://dx.doi.org/10.1016/j.cma.2016.02.021>, 2016.
- 5 Ai, M., Kong, X., and Li, K.: A general theory for orthogonal array based latin hypercube sampling, *Statistica Sinica*, 26, 761–777, <https://doi.org/doi:http://dx.doi.org/10.5705/ss.202015.0029>, <http://www3.stat.sinica.edu.tw/statistica/oldpdf/A26n217.pdf>, 2016.
- Akhavan-Safaei, A.: Analysis and Implementation of Multiple Models and Multi-Models for Shallow-Water Type Models of Large Mass Flows, Master's thesis, University at Buffalo, 2018.
- Allan, J.: Geology of the northern Colima and Zacoalco grabens, southwest Mexico: Late Cenozoic rifting in the Mexican volcanic belt, *Geological Society of America Bulletin*, 97, 473–485, <https://doi.org/10.1130/0016-7606>, 1986.
- 10 Bartelt, P. and McARDell, B.: Granulometric investigations of snow avalanches, *Journal of Glaciology*, 55, 829–833(5), 2009.
- Bartelt, P., Salm, B., and Gruber, U.: Calculating dense-snow avalanche runout using a Voellmy-fluid model with active/passive longitudinal straining, *Journal of Glaciology*, 45, 242–254, 1999.
- Bayarri, M. J., Berger, J. O., Calder, E. S., Dalbey, K., Lunagomez, S., Patra, A. K., Pitman, E. B., Spiller, E. T., and Wolpert, R. L.: Using
15 Statistical and Computer Models to Quantify Volcanic Hazards, *Technometrics*, 51, 402–413, <https://doi.org/10.1198/TECH.2009.08018>, <http://www.tandfonline.com/doi/abs/10.1198/TECH.2009.08018>, 2009.
- Bayarri, M. J., Berger, J. O., Calder, E. S., Patra, A. K., Pitman, E. B., Spiller, E. T., and Wolpert, R. L.: Probabilistic Quantification of Hazards: A Methodology Using Small Ensembles of Physics-Based Simulations and Statistical Surrogates, *International Journal for Uncertainty Quantification*, 5, 297–325, 2015.
- 20 Capra, L., Manea, V. C., Manea, M., and Norini, G.: The importance of digital elevation model resolution on granular flow simulations: a test case for Colima volcano using TITAN2D computational routine, *Natural Hazards*, 59, 665–680, <https://doi.org/10.1007/s11069-011-9788-6>, <https://doi.org/10.1007/s11069-011-9788-6>, 2011.
- Charbonnier, S. J. and Gertisser, R.: Numerical simulations of block-and-ash flows using the Titan2D flow model: examples from the 2006 eruption of Merapi Volcano, Java, Indonesia, *Bulletin of Volcanology*, 71, 953–959, <https://doi.org/10.1007/s00445-009-0299-1>, <https://doi.org/10.1007/s00445-009-0299-1>, 2009.
- 25 Christen, M., Kowalski, J., and Bartelt, P.: RAMMS: Numerical simulation of dense snow avalanches in three-dimensional terrain, *Cold Regions Science and Technology*, 63, 1–14, <https://doi.org/10.1016/j.coldregions.2010.04.005>, 2010.
- Cortés, A., Garduño, V., Navarro, C., Komorowski, J., Saucedo, R., Macías, J., and Gavilanes, J.: Geología del Complejo Volcánico de Colima., *Serie de Cartas y Mapas del Instituto de Geología*, 10, 37, 2005.
- 30 Cortés, A., Garduño, V., Navarro-Ochoa, C., Komorowski, J., Saucedo, R., Macías, J., and Gavilanes, J.: Geologic mapping of the Colima Volcanic Complex (Mexico), and implications for hazard assessment, *Geological Society of America, Special paper*, 464, 2010.
- Dade, W. B. and Huppert, H. E.: Long-runout rockfalls, *Geology*, 26, 803–806, <https://doi.org/10.1130/0091-7613>, 1998.
- Dalbey, K., Patra, A. K., Pitman, E. B., Bursik, M. I., and Sheridan, M. F.: Input uncertainty propagation methods and hazard mapping of geophysical mass flows, *Journal of Geophysical Research: Solid Earth*, 113, 1–16, <https://doi.org/10.1029/2006JB004471>, 2008.
- 35 Dalbey, K. R.: Predictive Simulation and Model Based Hazard Maps, Ph.D. thesis, University at Buffalo, 2009.
- Drucker, D. C. and Prager, W.: Soil mechanics and plastic analysis for limit design, *Quarterly of Applied Mathematics*, 10, 157–165, 1952.



- Farrell, K., Tinsley, J., and Faghihi, D.: A Bayesian framework for adaptive selection, calibration, and validation of coarse-grained models of atomistic systems, *Journal of Computational Physics*, 295, <https://doi.org/10.1016/J.JCP.2015.03.071>, 2015.
- Fischer, J., Kowalski, J., and Pudasaini, S. P.: Topographic curvature effects in applied avalanche modeling, *Cold Regions Science and Technology*, 74–75, 21–30, <https://doi.org/10.1016/j.coldregions.2012.01.005>, 2012.
- 5 Forterre, Y. and Pouliquen, O.: Stability analysis of rapid granular chute flows: formation of longitudinal vortices, *Journal of Fluid Mechanics*, 467, 361–387, 2002.
- Forterre, Y. and Pouliquen, O.: Long-surface-wave instability in dense granular flows., *Journal of Fluid Mechanics*, 486, 21–50, <https://doi.org/10.1017/S0022112003004555>, <http://dx.doi.org/10.1017/S0022112003004555>, 2003.
- Ghosh, T. and Krishnamurti, T. N.: Improvements in Hurricane Intensity Forecasts from a Multimodel Superensemble Utilizing a Generalized
10 Neural Network Technique, *Weather and Forecasting*, 33, 873–885, <https://doi.org/10.1175/WAF-D-17-0006.1>, 2018.
- Gilbert, S.: Model building and a definition of science, *Journal of Research in Science Teaching*, 28, 73–79, <https://doi.org/10.1002/tea.3660280107>, <https://onlinelibrary.wiley.com/doi/abs/10.1002/tea.3660280107>, 1991.
- Gruber, U. and Bartelt, P.: Snow avalanche hazard modelling of large areas using shallow water numerical models and GIS, *Environmental Modelling & Software*, 22, 1472–1481, <https://doi.org/10.1016/j.envsoft.2007.01.001>, 2007.
- 15 Iverson, R. M. and George, D. L.: A depth-averaged debris-flow model that includes the effects of evolving dilatancy. I. Physical basis, *Proceedings of the Royal Society of London A: Mathematical, Physical and Engineering Sciences*, 470, <https://doi.org/10.1098/rspa.2013.0819>, <http://rspa.royalsocietypublishing.org/content/470/2170/20130819>, 2014.
- Kelfoun, K.: Suitability of simple rheological laws for the numerical simulation of dense pyroclastic flows and long-runout volcanic avalanches, *Journal of Geophysical Research*, 116, B08 209, <https://doi.org/10.1029/2010JB007622>, 2011.
- 20 Kern, M., Bartelt, P., Sovilla, B., and Buser, O.: Measured shear rates in large dry and wet snow avalanches, *Journal of Glaciology*, 55, 327–338, 2009.
- Krishnamurti, T. N., Kumar, V., Simon, A., Bhardwaj, A., Ghosh, T., and Ross, R.: A review of multimodel superensemble forecasting for weather, seasonal climate, and hurricanes, *Reviews of Geophysics*, 54, 336–377, <https://doi.org/10.1002/2015RG000513>, <https://agupubs.onlinelibrary.wiley.com/doi/abs/10.1002/2015RG000513>, 2016.
- 25 Luhr, J. and Carmichael, J.: Geology of the Volán de Colima, Serie de Divulgación, Universidad Nacional de México, Instituto de Geología, 1990.
- Macorps, E., Charbonnier, S. J., Varley, N. R., Capra, L., Atlas, Z., and Cabré, J.: Stratigraphy, sedimentology and inferred flow dynamics from the July 2015 block-and-ash flow deposits at Volcán de Colima, Mexico, *Journal of Volcanology and Geothermal Research*, 349, 99 – 116, <https://doi.org/https://doi.org/10.1016/j.jvolgeores.2017.09.025>, <http://www.sciencedirect.com/science/article/pii/S0377027317301129>, 2018.
- 30 McKay, M. D., Beckman, R. J., and Conover, W. J.: A comparison of three methods for selecting values of input variables in the analysis of output from a computer code, *Technometrics*, 21, 239–245, <http://www.jstor.org/stable/1268522>, 1979.
- Mooser, F.: Los volcanes de Colima, vol. 61, pp. 49–71, Universidad Nacional Autónoma de México, Instituto de Geología, 1961.
- NASA (JPL): U.S. Releases Enhanced Shuttle Land Elevation Data, Shuttle Radar Topography Mission (SRTM), Tech. rep., NASA, <https://www2.jpl.nasa.gov/srtm/>, 2014.
- 35 Norini, G., De Beni, E., Andronico, D., Polacci, M., Burton, M., and Zucca, F.: The 16 November 2006 flank collapse of the south-east crater at Mount Etna, Italy: Study of the deposit and hazard assessment, *Journal of Geophysical Research: Solid Earth*, 114, <https://doi.org/10.1029/2008JB005779>, <http://dx.doi.org/10.1029/2008JB005779>, b02204, 2009.



- Ogburn, S. E., Berger, J., Calder, E. S., Lopes, D., Patra, A., Pitman, E. B., Rutarindwa, R., Spiller, E., and Wolpert, R. L.: Pooling strength amongst limited datasets using hierarchical Bayesian analysis, with application to pyroclastic density current mobility metrics, *Statistics in Volcanology*, 2, 1–26, <https://doi.org/http://dx.doi.org/10.5038/2163-338X.2.1>, 2016.
- Owen, A. B.: Orthogonal arrays for computer experiments, integration and visualization, *Statistica Sinica*, 2, 439–452, <http://www.jstor.org/stable/24304869>, 1992a.
- Owen, A. B.: A Central Limit Theorem for Latin Hypercube Sampling, *Journal of the Royal Statistical Society.*, 54, 541–551, 1992b.
- Patra, A., Nichita, C., Bauer, A., Pitman, E., Bursik, M., and Sheridan, M.: Parallel adaptive discontinuous Galerkin approximation for thin layer avalanche modeling, *Computers & Geosciences*, 32, 912 – 926, <https://doi.org/https://doi.org/10.1016/j.cageo.2005.10.023>, <http://www.sciencedirect.com/science/article/pii/S0098300405002736>, computer Simulation of natural phenomena for Hazard Assessment, 2006.
- Patra, A., Bevilacqua, A., and Akhavan-Safaei, A.: Analyzing Complex Models using Data and Statistics, vol. 10861 of *ICCS, Lecture Notes in Computer Science*, chap. 57, pp. 724–736, Springer, ISBN 978-3-319-93701-4, 2018a.
- Patra, A., Bevilacqua, A., Akhavan-Safaei, A., Pitman, E., Bursik, M., and Hyman, D.: Comparative analysis of the structures and outcomes of geophysical flow models and modeling assumptions using uncertainty quantification, *arXiv.org*, 1805.12104, 1–39, 2018b.
- Patra, A. K., Bauer, A. C., Nichita, C. C., Pitman, E. B., Sheridan, M. F., Bursik, M., Rupp, B., Webber, A., Stinton, A. J., Namikawa, L. M., and Renschler, C. S.: Parallel adaptive numerical simulation of dry avalanches over natural terrain, *Journal of Volcanology and Geothermal Research*, 139, 1–21, <https://doi.org/10.1016/j.jvolgeores.2004.06.014>, <http://linkinghub.elsevier.com/retrieve/pii/S0377027304002288>, 2005.
- Pierson, T.: Initiation and flow behavior of the 1980 pine creek and Muddy River lahars, Mont St. Helens, Washington, *Geological Society of America Bulletin*, 96, 1056–1069, 1985.
- Pitman, E. B. and Le, L.: A two-fluid model for avalanche and debris flows, *Philosophical transactions. Series A, Mathematical, physical, and engineering sciences*, 363, 1573–601, <https://doi.org/10.1098/rsta.2005.1596>, <http://www.ncbi.nlm.nih.gov/pubmed/16011934>, 2005.
- Ponce-Segura, J.: *Historia de Atenquique*, Talleres litográficos Vera, Guadalajara, Jalisco, México, 1983.
- Popper, K. R.: *The Logic of Scientific Discovery*, Routledge, <https://doi.org/10.2307/2104331>, 1959.
- Pouliquen, O.: Scaling laws in granular flows down rough inclined planes, *Physics of Fluids*, 11, 542–548, 1999.
- Pouliquen, O. and Forterre, Y.: Friction law for dense granular flows: application to the motion of a mass down a rough inclined plane, *Journal of Fluid Mechanics*, 453, 133–151, <https://doi.org/10.1017/S0022112001006796>, 2002.
- Procter, J. N., Cronin, S. J., Platz, T., Patra, A., Dalbey, K., Sheridan, M., and Neall, V.: Mapping block-and-ash flow hazards based on Titan 2D simulations: a case study from Mt. Taranaki, NZ, *Natural Hazards*, 53, 483–501, <https://doi.org/10.1007/s11069-009-9440-x>, <https://doi.org/10.1007/s11069-009-9440-x>, 2010.
- Pudasaini, S. P. and Hutter, K.: Rapid shear flows of dry granular masses down curved and twisted channels, *Journal of Fluid Mechanics*, 495, 193–208, 2003.
- Ranjan, P. and Spencer, N.: Space-filling Latin hypercube designs based on randomization restrictions in factorial experiments, *Statistics and Probability Letters*, 94, 239 – 247, <https://doi.org/https://doi.org/10.1016/j.spl.2014.07.032>, <http://www.sciencedirect.com/science/article/pii/S016771521400279X>, 2014.
- Rankine, W. J. M.: On the Stability of Loose Earth, *Phil. Trans. R. Soc. Lond.*, 147, 9–27, 1857.



- Robin, C., Mossand, P., Camus, G., Cantagrel, J., Gourgaud, A., and Vincent, P.: Eruptive history of the Colima volcanic complex (Mexico), *Journal of Volcanology and Geothermal Research*, 31, 99 – 113, [https://doi.org/https://doi.org/10.1016/0377-0273\(87\)90008-4](https://doi.org/https://doi.org/10.1016/0377-0273(87)90008-4), <http://www.sciencedirect.com/science/article/pii/0377027387900084>, 1987.
- Rupp, B.: An analysis of granular flows over natural terrain, Master's thesis, University at Buffalo, 2004.
- 5 Rupp, B., Bursik, M., Namikawa, L., Webb, A., Patra, A. K., Saucedo, R., Macías, J. L., and Renschler, C.: Computational modeling of the 1991 block and ash flows at Colima Volcano, Mexico, *Geological Society of America Special Papers*, 402, 223–237, [https://doi.org/10.1130/2006.2402\(11\)](https://doi.org/10.1130/2006.2402(11)), 2006.
- Salm, B.: Flow, flow transition and runout distances of flowing avalanches, *Annals of Glaciology*, 18, 221–226, 1993.
- Salm, B., Burkard, A., and Gubler, H.: Berechnung von Fliesslawinen: eine Anleitung für Praktiker mit Beispielen, *Mitteilungen des Eidgenössische Institutes für Schnee- und Lawinenforschung*, 47, 1990.
- 10 Saucedo, R.: The 1955 debris flow generated by intense rain fall at Atenquique, Jalisco, Mexico, in: *Regional Geomorphology Conference*, Mexico City, Mexico, 2003.
- Saucedo, R., Macías, J. L., Sarocchi, D., Bursik, M., and Rupp, B.: The rain-triggered Atenquique volcanoclastic debris flow of October 16, 1955 at Nevado de Colima Volcano, Mexico, *Journal of Volcanology and Geothermal Research*, 173, 69–83, 2008.
- 15 Saucedo, R., Macías, J., Gavilanes, J., Arce, J., Komorowski, J., Gardner, J., and Valdez-Moreno, G.: Eyewitness, stratigraphy, chemistry, and eruptive dynamics of the 1913 Plinian eruption of Volcán de Colima, México, *Journal of Volcanology and Geothermal Research*, 191, 149 – 166, <https://doi.org/https://doi.org/10.1016/j.jvolgeores.2010.01.011>, <https://www.sciencedirect.com/science/article/pii/S0377027310000259>, 2010.
- Savage, S. B. and Hutter, K.: The motion of a finite mass of granular material down a rough incline, *Journal of Fluid Mechanics*, 199, 177, <https://doi.org/10.1017/S0022112089000340>, http://journals.cambridge.org/article_S0022112089000340, 1989.
- 20 Sheridan, M., Stinton, A., Patra, A., Pitman, E., Bauer, A., and Nichita, C.: Evaluating Titan2D mass-flow model using the 1963 Little Tahoma Peak avalanches, Mount Rainier, Washington, *Journal of Volcanology and Geothermal Research*, 139, 89 – 102, <https://doi.org/https://doi.org/10.1016/j.jvolgeores.2004.06.011>, <http://www.sciencedirect.com/science/article/pii/S0377027304002331>, modeling and Simulation of Geophysical Mass Flows, 2005.
- 25 Sheridan, M. F., Patra, A. K., Dalbey, K., and Hubbard, B.: Probabilistic digital hazard maps for avalanches and massive pyroclastic flows using TITAN2D, vol. *Stratigraphy and geology of volcanic areas*, 464, chap. 14, p. 281, Geological Society of America, 2010.
- Spiller, E. T., Bayarri, M. J., Berger, J. O., Calder, E. S., Patra, A. K., Pitman, E. B., and Wolpert, R. L.: Automating Emulator Construction for Geophysical Hazard Maps, *SIAM/ASA Journal on Uncertainty Quantification*, 2, 126–152, <https://doi.org/10.1137/120899285>, <http://dx.doi.org/10.1137/120899285>, 2014.
- 30 Stefanescu, E. R., Bursik, M., Cordoba, G., Dalbey, K., Jones, M. D., Patra, A. K., Pieri, D. C., Pitman, E. B., and Sheridan, M. F.: Digital elevation model uncertainty and hazard analysis using a geophysical flow model, *Proceedings of the Royal Society of London A: Mathematical, Physical and Engineering Sciences*, 468, 1543–1563, <https://doi.org/10.1098/rspa.2011.0711>, <http://rspa.royalsocietypublishing.org/content/468/2142/1543>, 2012a.
- Stefanescu, E. R., Bursik, M., and Patra, A. K.: Effect of digital elevation model on Mohr-Coulomb geophysical flow model output, *Natural Hazards*, 62, 635–656, <https://doi.org/10.1007/s11069-012-0103-y>, <https://doi.org/10.1007/s11069-012-0103-y>, 2012b.
- 35 Stein, M.: Large Sample Properties of Simulations Using Latin Hypercube Sampling, *Technometrics*, 29, 143–151, <http://www.jstor.org/stable/1269769>, 1987.



- Sulpizio, R., Capra, L., Sarocchi, D., Saucedo, R., Gavilanes-Ruiz, J., and Varley, N.: Predicting the block-and-ash flow inundation areas at Volcán de Colima (Colima, Mexico) based on the present day (February 2010) status, *Journal of Volcanology and Geothermal Research*, 193, 49 – 66, <https://doi.org/https://doi.org/10.1016/j.jvolgeores.2010.03.007>, <http://www.sciencedirect.com/science/article/pii/S0377027310000983>, 2010.
- 5 Tang, B.: Orthogonal Array-Based Latin Hypercubes, *Journal of the American Statistical Association*, 88, 1392–1397, <http://www.jstor.org/stable/2291282>, 1993.
- Tarantola, A.: *Inverse Problem Theory: Methods for Data Fitting and Model Parameter Estimation*, Elsevier, 1987.
- Tarantola, A. and Valette, B.: Inverse Problems = Quest for Information, *Journal of Geophysics*, 50, 159–170, 1982.
- Voellmy, A.: Über die Zerstörungskraft von Lawinen, *Schweiz Bauzeitung*, 73, 159–165, 212–217, 246–249, 280–285, 1955.
- 10 Yu, B., Dalbey, K., Webb, A., Bursik, M., Patra, A. K., Pitman, E. B., and Nichita, C.: Numerical issues in computing inundation areas over natural terrains using Savage-Hutter theory, *Natural Hazards*, 50, 249–267, <https://doi.org/10.1007/s11069-008-9336-1>, <http://link.springer.com/article/10.1007/s11069-008-9336-1>, 2009.
- Zobin, V., Arámbula, R., Bretón, M., Reyes, G., Plascencia, I., Navarro, C., Téllez, A., Campos, A., González, M., León, Z., Martínez, A., and Ramírez, C.: Dynamics of the January 2013–June 2014 explosive-effusive episode in the eruption of Volcán de Colima, México: insights from seismic and video monitoring, *Bulletin of Volcanology*, 77, 31, <https://doi.org/10.1007/s00445-015-0917-z>, <https://doi.org/10.1007/s00445-015-0917-z>, 2015.
- 15